16552-6008-R0-00
CR 114351
AVAILABLE TO THE PUBLIC

STUDY OF A COMMON SOLAR-ELECTRIC-PROPULSION UPPER STAGE FOR HIGH-ENERGY UNMANNED MISSIONS

VOLUME III
APPENDIXES

PREPARED FOR NASA/OART
ADVANCED CONCEPTS AND MISSIONS DIVISION
MOFFETT FIELD, CALIFORNIA

UNDER CONTRACT NAS2-6040

14 JULY 1971

TRW SYSTEMS GROUP

16552-6008-R0-00

STUDY OF A COMMON SOLAR-ELECTRIC-PROPULSION UPPER STAGE FOR HIGH-ENERGY UNMANNED MISSIONS

VOLUME III
APPENDIXES

PREPARED FOR NASA/OART
ADVANCED CONCEPTS AND MISSIONS DIVISION
MOFFETT FIELD, CALIFORNIA

UNDER CONTRACT NAS2-6040

14 JULY 1971

TRW
SYSTEMS GROUP

The final report of this study
is presented in three volumes:

I Summary Report
II Technical Report
III Appendix

ABSTRACT

The results of this study show that the multi-mission solar-electric stage concept is a practical, economical, and versatile approach to space exploration. A vehicle designed for repeated use in a variety of missions permits amortization of development and reduction of recurring cost. The upper stage concept affords additional cost savings because new development for any mission is largely restricted to payload engineering.

The selected configuration consists of a center body and two rollout solar arrays developing 17.5 kw at 1 AU. The vehicle, launched by a Titan class booster, has an injected mass ranging from 1500 to 2500 kg and carries up to 500 kg of attached or separable payload packages. A large payload stowage volume is provided.

High-energy missions to be performed by this stage starting in the mid-70's are those where solar-electric power can be used most effectively, namely a Mercury orbiter, a close approach solar probe, asteroid and comet rendezvous missions, and a high-inclination extra-ecliptic probe. Alternate missions to which the stage can be adapted are high-data-rate Mars and Venus orbiters, and outer planet flybys and orbiters. Still more advanced missions such as surface sample return from Mars or the asteroid Eros, and the very difficult rendezvous with Halley's comet in 1986 have also been suggested.

TRW Systems has analyzed mission characteristics, scientific objectives and payload requirements, performed design tradeoffs and interface studies, and defined a conceptual stage configuration that meets the specified wide range of mission objectives. The study also includes program plans and cost estimates and identifies advanced technology development that will be required for implementing the electric stage program.

TABLE OF CONTENTS

APPENDIXES

LIST OF ILLUSTRATIONS

APPENDIXES

LIST OF ILLUSTRATIONS (Continued)

APPENDIXES

LIST OF ILLUSTRATIONS (Continued)

APPENDIXES

LIST OF TABLES

APPENDICES

APPENDIX A

INFLUENCE OF SPECIFIC IMPULSE ON PAYLOAD CAPACITY

As discussed in Section 5.4 of the Technical Report, the initial trajectory study determined reference characteristics based on unconstrained optimal specific impulse, I_{sp}, or exhaust velocity C, of the electric thrusters, where optimality refers to maximum net spacecraft mass that can be attained for a specified mission duration and power level. In many instances, especially with a low power level, the unconstrained optimal I_{sp} value is well below the lower limit attainable by present or future electric thruster technology.

Figure A-1 shows the theoretical optimum exhaust velocity C as function of power level for each of the five primary missions at the selected nominal mission time. In three of these missions the exhaust velocity, or specific impulse, falls to unrealizable values ($I_{sp} < 2500$ sec) at power levels in the 15 to 30 kw range. This means that the (unconstrained) optimization procedure seeks to obtain a higher thrust per unit power by lowering the specific impulse level.

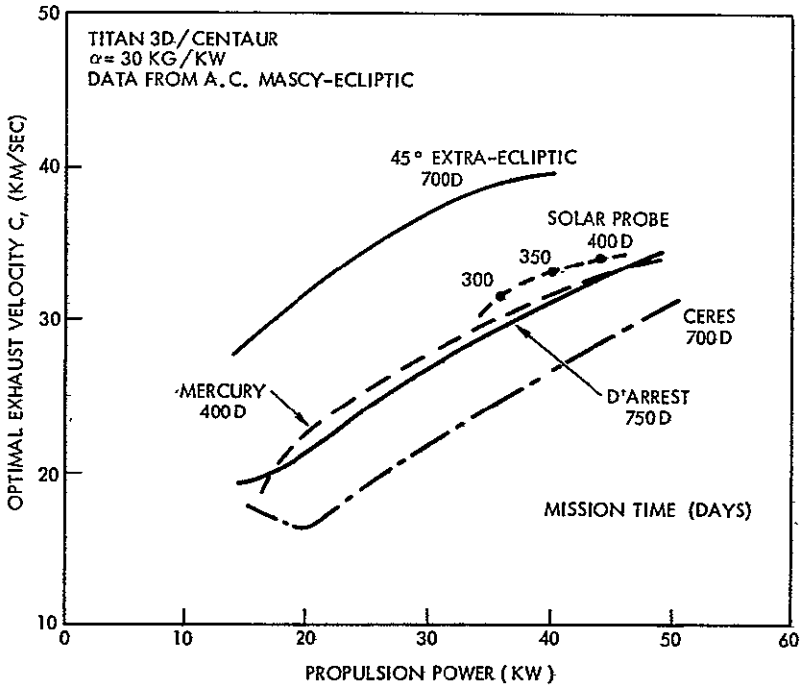

Figure A-1. Variation of Optimal Specific Impulse

Figure A-2 shows the variation of payload capacity that results from a change in specific impulse from the theoretical optimum in four of the primary missions. Except for the case of the extra-ecliptic mission the payload is quite sensitive to the departure from the optimum I_{sp}. Operation at I_{sp} = 3000 sec, the lower limit of available thruster technology, results in a 25 percent lower net spacecraft mass in the example of the Ceres mission. Other examples of the effect of I_{sp} selection on payload were previously shown in Figures 5-6 and 5-7 (Section 5.4).

The strong influence of I_{sp} on payload mass, especially in rendezvous missions, can be explained by comparing the mass characteristics for a 700-day Ceres mission in which the theoretical optimum I_{sp} (1860 sec) and a practical I_{sp} (3000 sec) are used, see Table A-1. A power level of 15 kw at 1 AU is assumed.

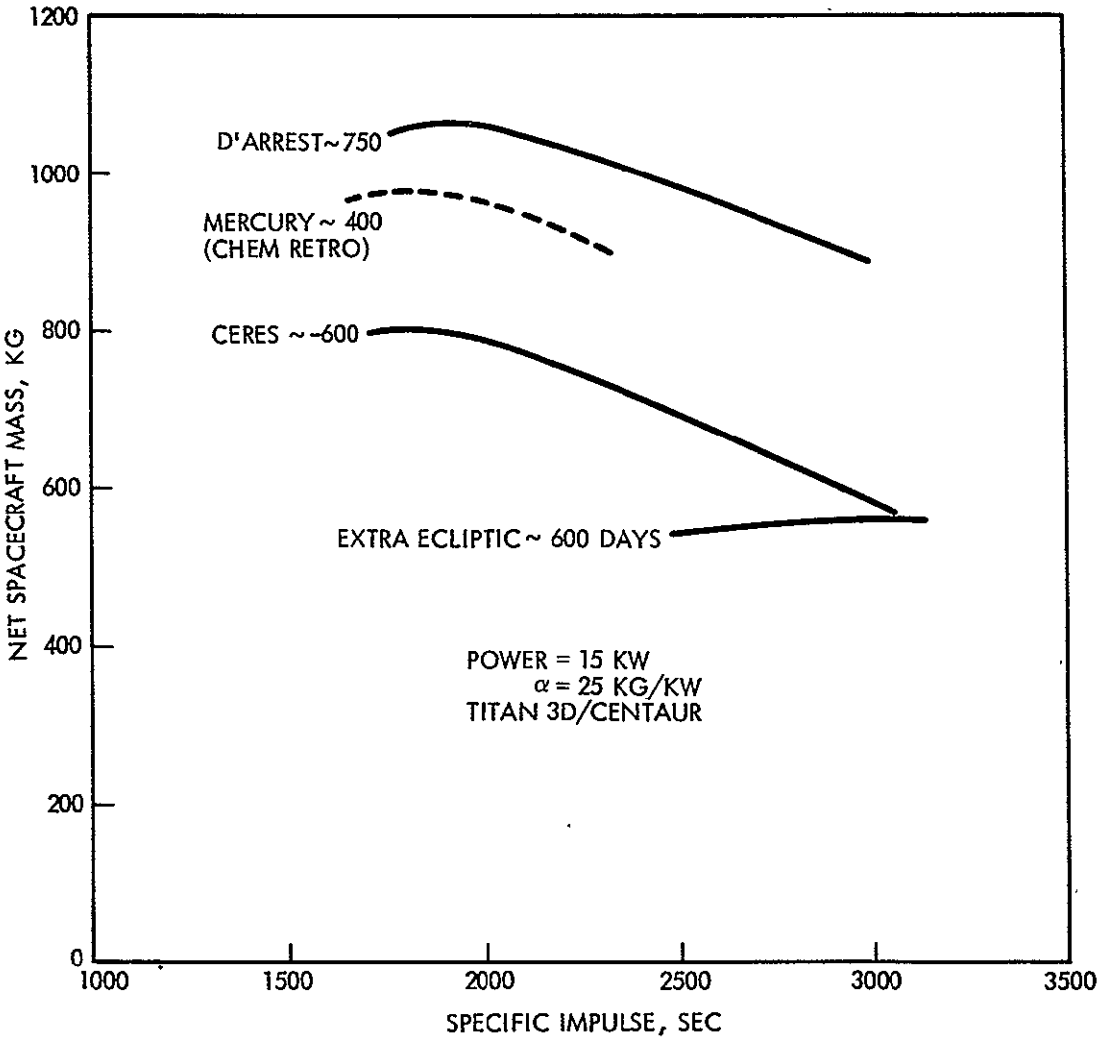

Figure A-2. Net Spacecraft Mass Variation with Specific Impulse

Table A-1. Comparison of Mass Characteristics for Theoretical Optimum and Actual Specific Impulse*

Characteristics	Optimum I_{sp} 1860 Sec $\eta = 0.505$	Actual I_{sp} 3000 Sec $\eta = 0.636$
Departure hyperbolical velocity (km/sec)	7.0	8.5
Nominal injected mass (kg)	2437	1589
Solar array and electric propulsion mass	450	450
Propellant mass	1060	456
Net spacecraft mass	891	659
Initial power-to-mass ratio (kw/kg)	6.15×10^{-3}	9.45×10^{-3}
Terminal power-to-mass ratio (kw/kg)	1.86×10^{-3}	2.26×10^{-3}
Initial acceleration (micro-g)	36.6	42
Terminal acceleration (micro-g)	10.5	10

*Ceres Rendezvous, 700 days; Titan 3D/Centaur α = 30 kg/kw; P_o = 15 kw)

To explain the reduction of payload mass with increase in I_{sp} we consider the propellant flow rate

$$\dot{M}_{prop} = \frac{2P_o\eta}{I_{sp}^2}$$

and its effect on final stage mass and acceleration capability. Since $\dot{M}_{prop}$ varies in inverse proprtions with I_{sp}^2/η, an increase of I_{sp} from 1860 to 3000 sec, with a corresponding increase in efficiency from 56 to 70 percent, has the effect of reducing the flow rate by a factor of 2.2. Therefore, as a result of using a larger I_{sp} value the stage mass at the end of the mission is larger than for low I_{sp}, the thrust force is smaller and the available acceleration is greatly reduced. To complete the rendezvous mission successfully within the specified time at the given power level a reduction of the initial stage mass is required, as seen in Table A-1. However, since the electric propulsion mass and solar array mass is fixed, any reduction of the initial gross mass necessitated by the larger I_{sp} value has a large leverage in reducing the net spacecraft mass.

A related aspect of the strong dependence of mass characteristics on initial acceleration is exhibited in Figure A-3, which shows the sensitive changes of power, payload mass, and injected mass that correspond to very small acceleration changes of only 10 percent for a given mission time. These data are derived from the optimum payload results obtained by Mascy.

In missions without a target rendezvous requirement, i.e., flyby or area missions, the effect of a major I_{sp} change is much less critical as seen by the results of the out-of-ecliptic mission (Section 5.4) and data on outer planet flyby missions published in a recent paper by Bartz and Horsewood.*

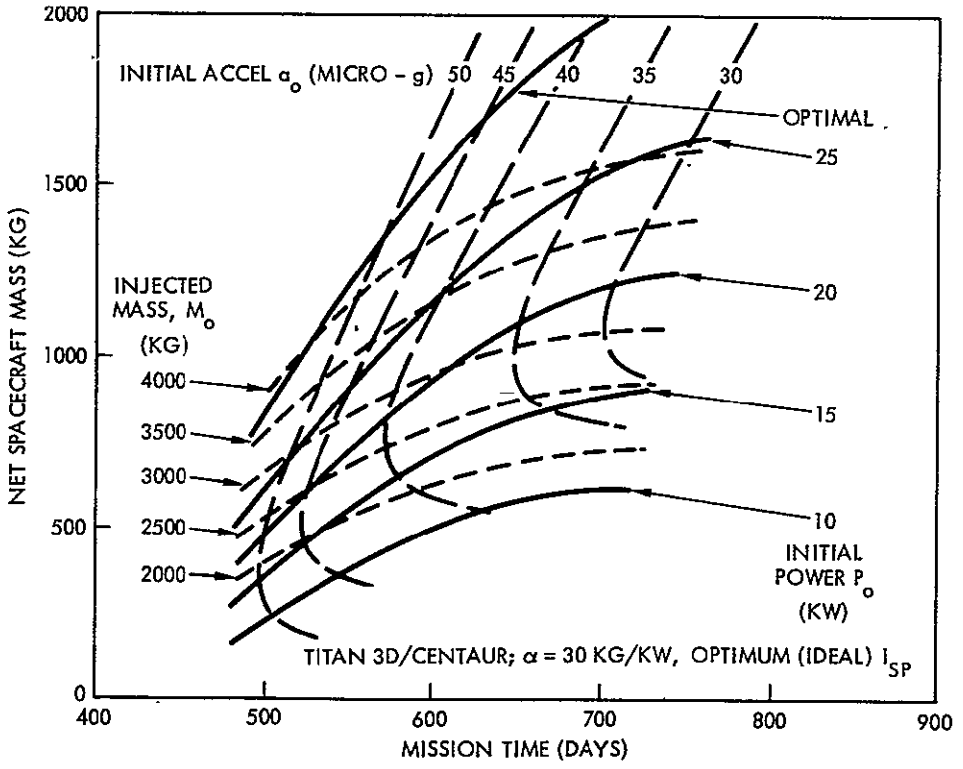

Figure A-3. Variation of Net Spacecraft Mass with Power and Initial Acceleration as a Function of Mission Time

*Bartz, D. R., and Horsewood, J. L., "Characteristics, Capabilities, and Costs of Solar Electric Spacecraft for Planetary Missions," AIAA Report No. 69-1103 presented at AIAA 6th Annual Meeting and Technical Display, Anaheim, California, October 20-24, 1969.

APPENDIX B

ADDITIONAL CHARACTERISTICS OF NOMINAL MISSION PROFILES

This appendix presents additional data of the nominal mission profiles previously discussed in Section 5.7 of the Technical Report, see Figures 5-16 through 5-21. For each of these missions target orbital elements (as applicable), electric stage characteristics and flight dates are summarized, and time histories of heliocentric longitude and latitude, optimum thrust steering angles (clock and cone angles) and sun-earth-probe geometry characteristics are shown (Figures B-1 through B-17).

In the design study we used these mission data to derive antenna pointing requirements, telemetry data rate capabilities, and thrust steering requirements, in plane and out of plane. The steering angle time history for each mission also indicates the orientation of the hyperbolic velocity vector which coincides with the initial thrust vector orientation.

SUMMARY - ASTEROID CERES RENDEZVOUS

Orbital Elements

$a = 2.768$ AU	Semi-Major Axis
$e = 0.076$	Eccentricity
$i = 10.61^{o}$	Inclination
$\Omega = 80.51^{o}$	Ascending Node
$\tilde{\omega} = \omega + \Omega = 152.37^{o}$	Longitude of Perihelion
$\lambda^{*} = 52.37^{o}$	Mean Longitude of Epoch
$T^{*} = 2440953$	Epoch - Julian Date

Launch Vehicle Titan 3D/Centaur

SEP Stage

(Optimal Pointing)

- Net Payload (Science) 259 KG
- Net Spacecraft 659 KG
- Injection Mass (M_o) 1589 KG
- Propellant Frac (M_p/M_o) 0.293
- Powerplant Frac (M_{pp}/M_o) 0.283
- Tank = 3% M_p
- α = 30 KG/KW
- Power = 15 KW
- I_{SP} = 3000 Sec (η = 0.636)

Earth Departure	October 8, 1976	V_∞ = 8.5 KM/SEC
Target Arrival	September 8, 1978	V_∞ = 0
Trip Time	700 Days	
Thrust Time	671 Days	

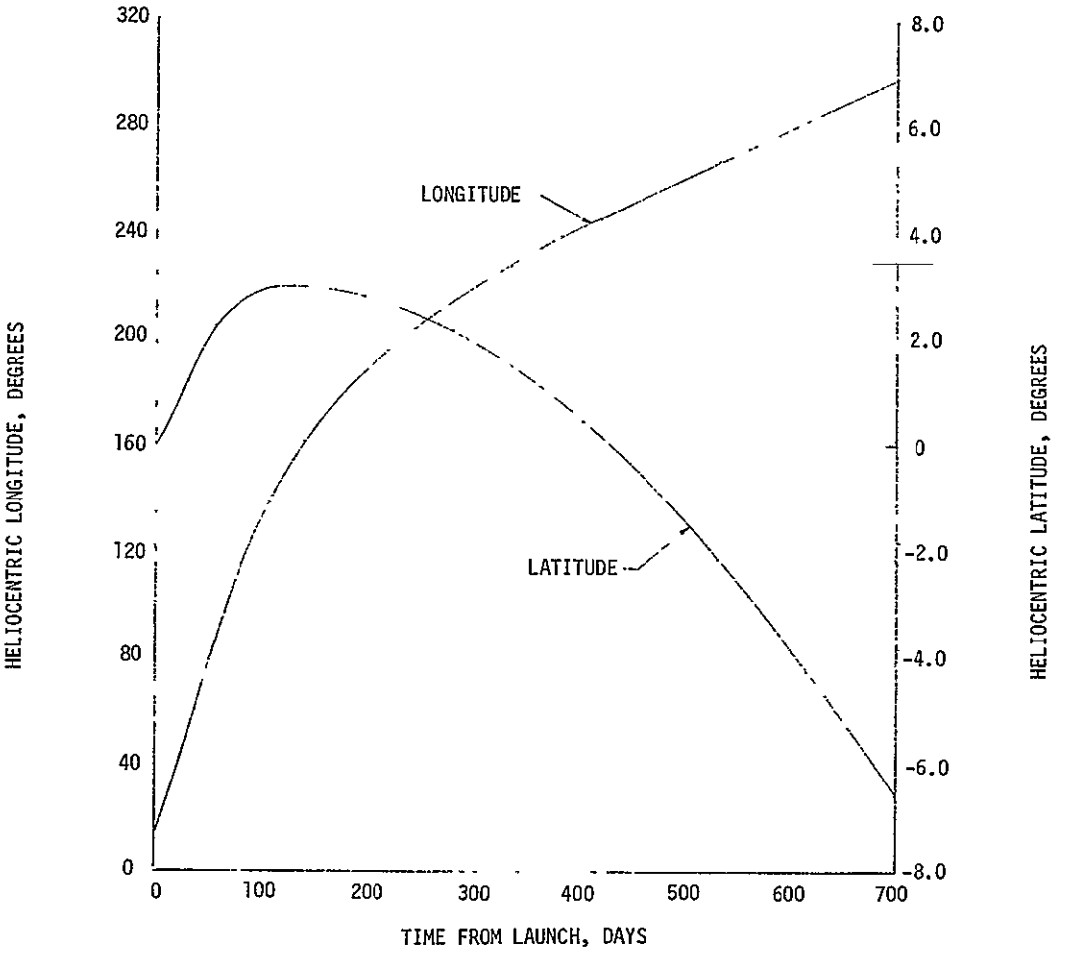

Figure B-1. Probe Position Angles (Ceres Rendezvous Mission)

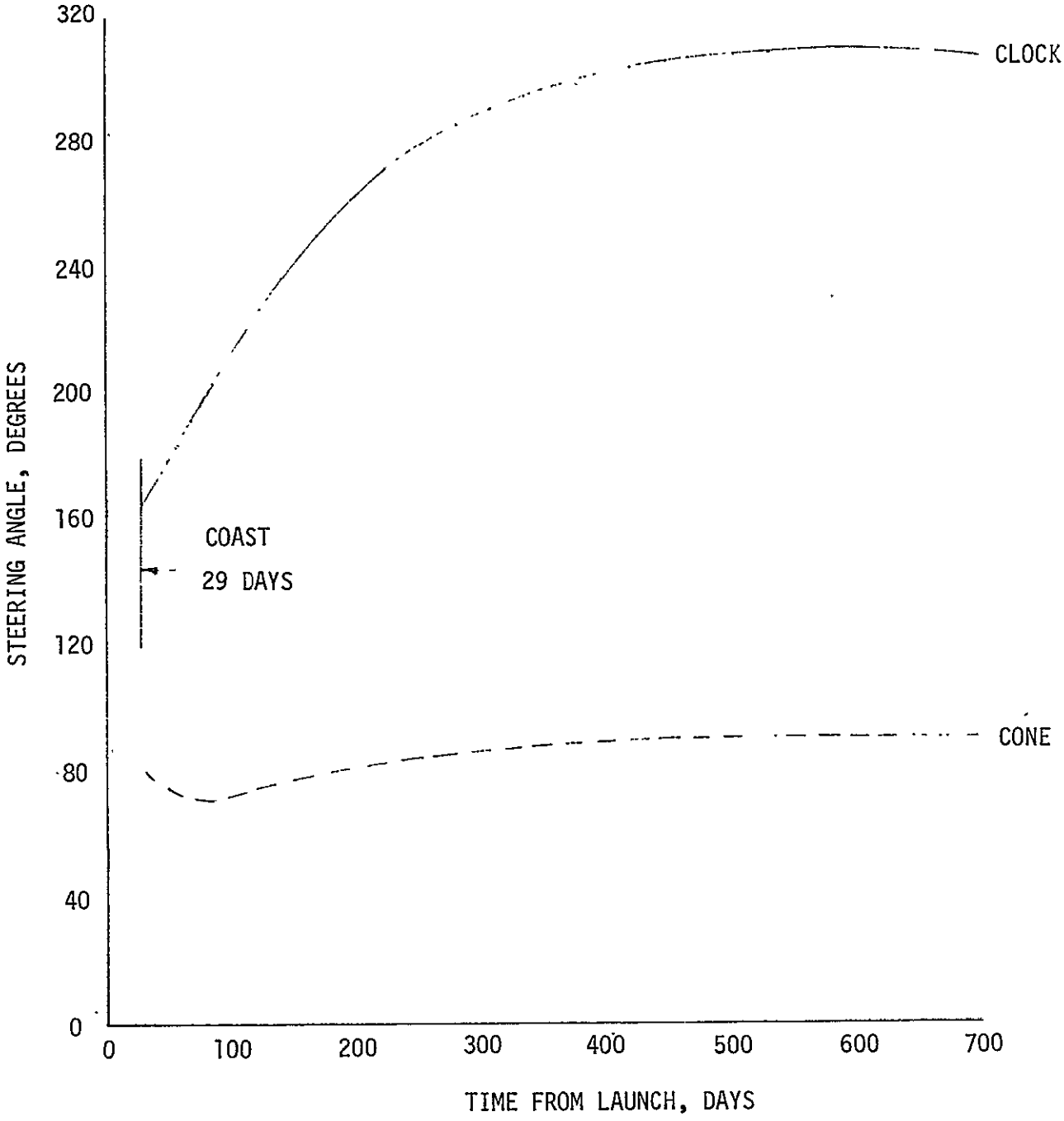

Figure B-2. Optimal Variable Steering Angle History (Ceres Rendezvous Mission)

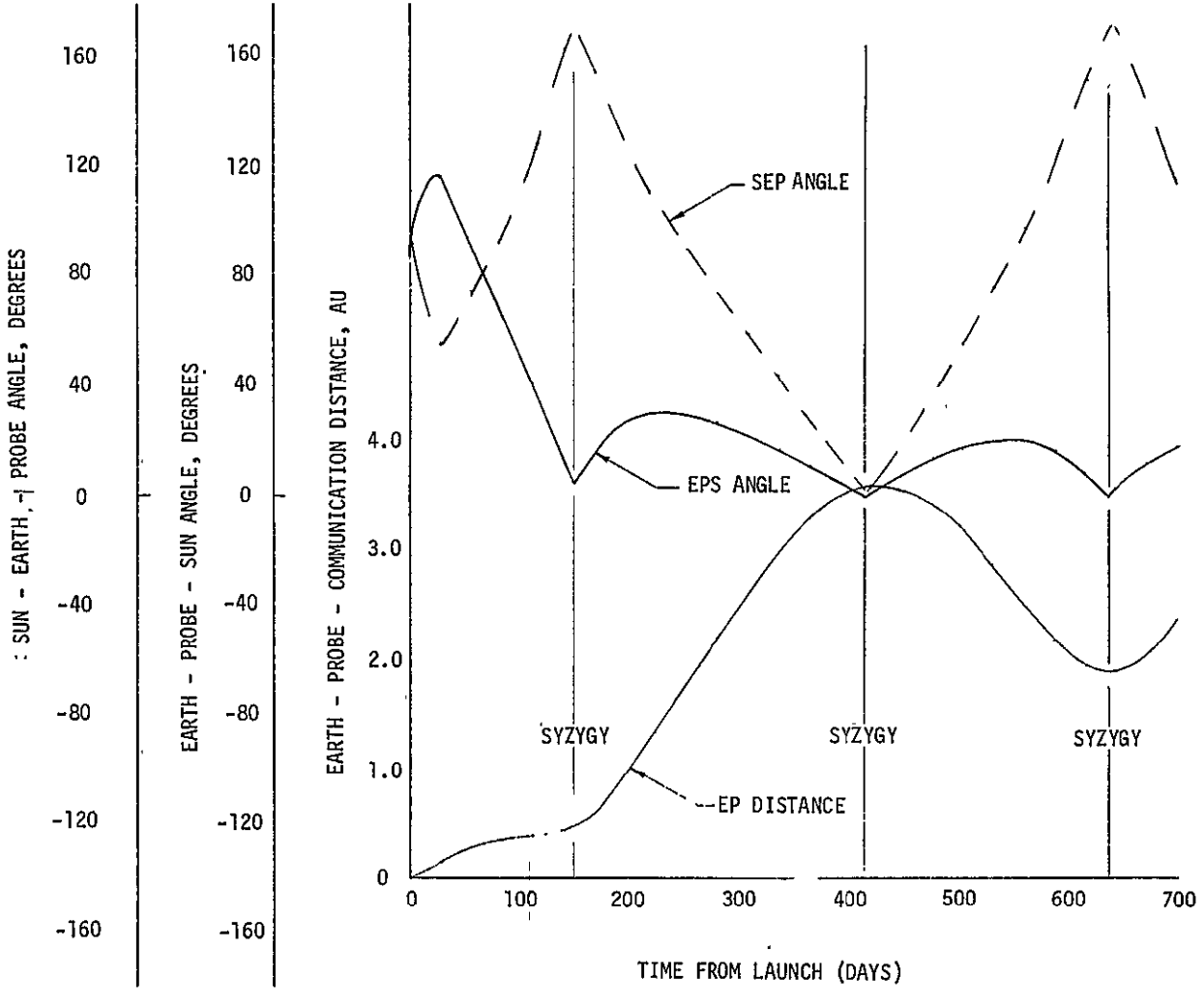

Figure B-3. Mission Data for Communications (Ceres Rendezvous Mission)

SUMMARY - COMET D'ARREST RENDEZVOUS

Orbital Elements

$a = 3.448$ AU
$e = 0.623$
$i = 19.61^{o}$
$\Omega = 138.98^{o}$
$\tilde{\omega} = \omega + \Omega = 315.83^{o}$
$\lambda^* = 315.83^{o}$
$T^* = 2445230$

Launch Vehicle Titan 3D/Centaur

SEP Stage
(Optimal Pointing)

- Net Payload (Science) 365 KG
- Net Spacecraft 811 KG
- Injection Mass (M_o) 1859 KG
- Propellant Frac (M_p/M_o) 0.312
- Powerplant Frac (M_{pp}/M_o) 0.242
- Tank = 3% M_p
- α = 30 KG/KW
- Power = 15 KW
- I_{SP} = 3000 SEC (η = 0.636)

Earth Departure	August 28, 1980	V_∞ = 8.0 KM/SEC
Target Arrival	September 17, 1982	V_∞ = 0
Trip Time	750 Days	
Thrust Time	704 Days	

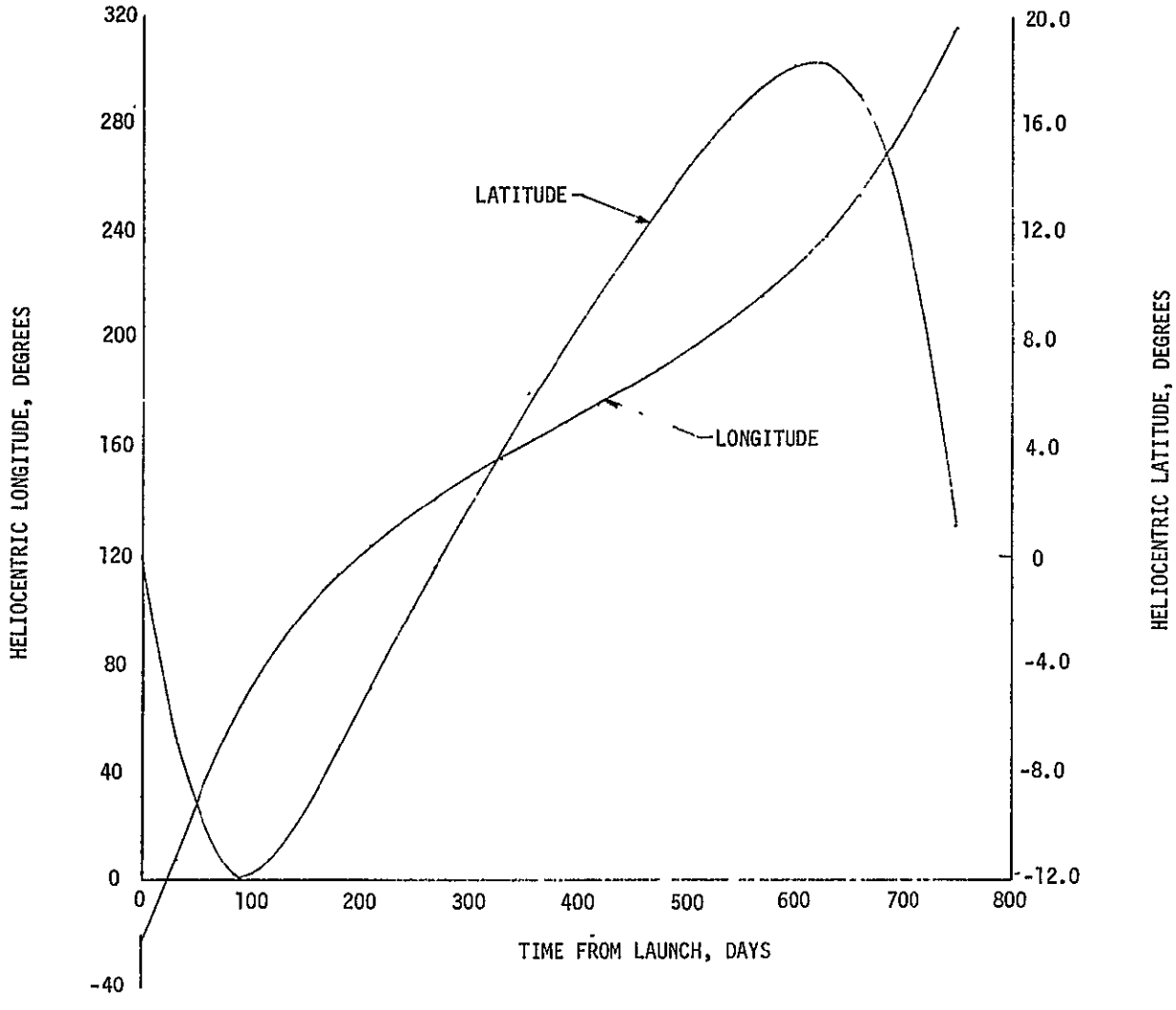

Figure B-4. Probe Position Angles
(Comet D'Arrest Rendezvous Mission)

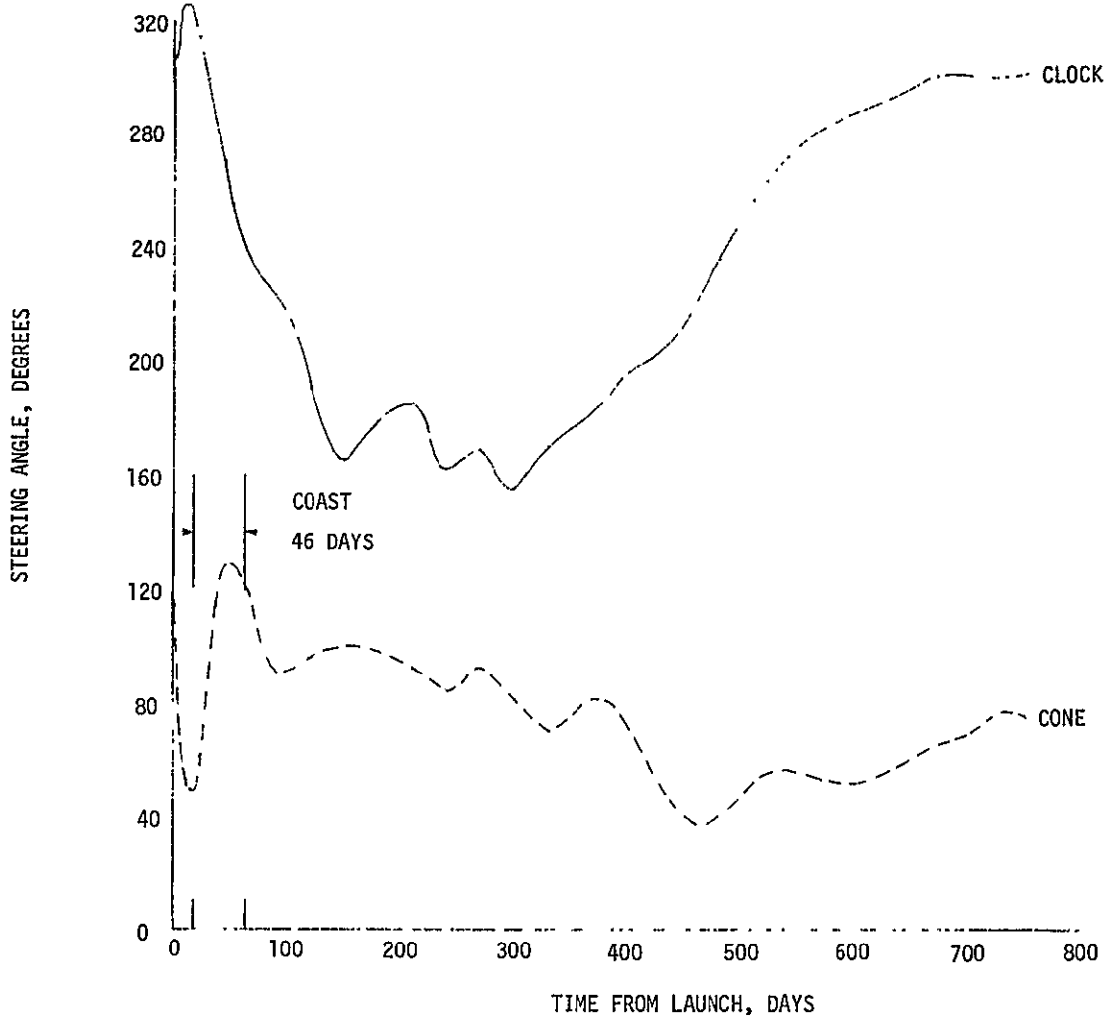

Figure B-5. Optimal Variable Steering Angle History (Comet D'Arrest Rendezvous Mission)

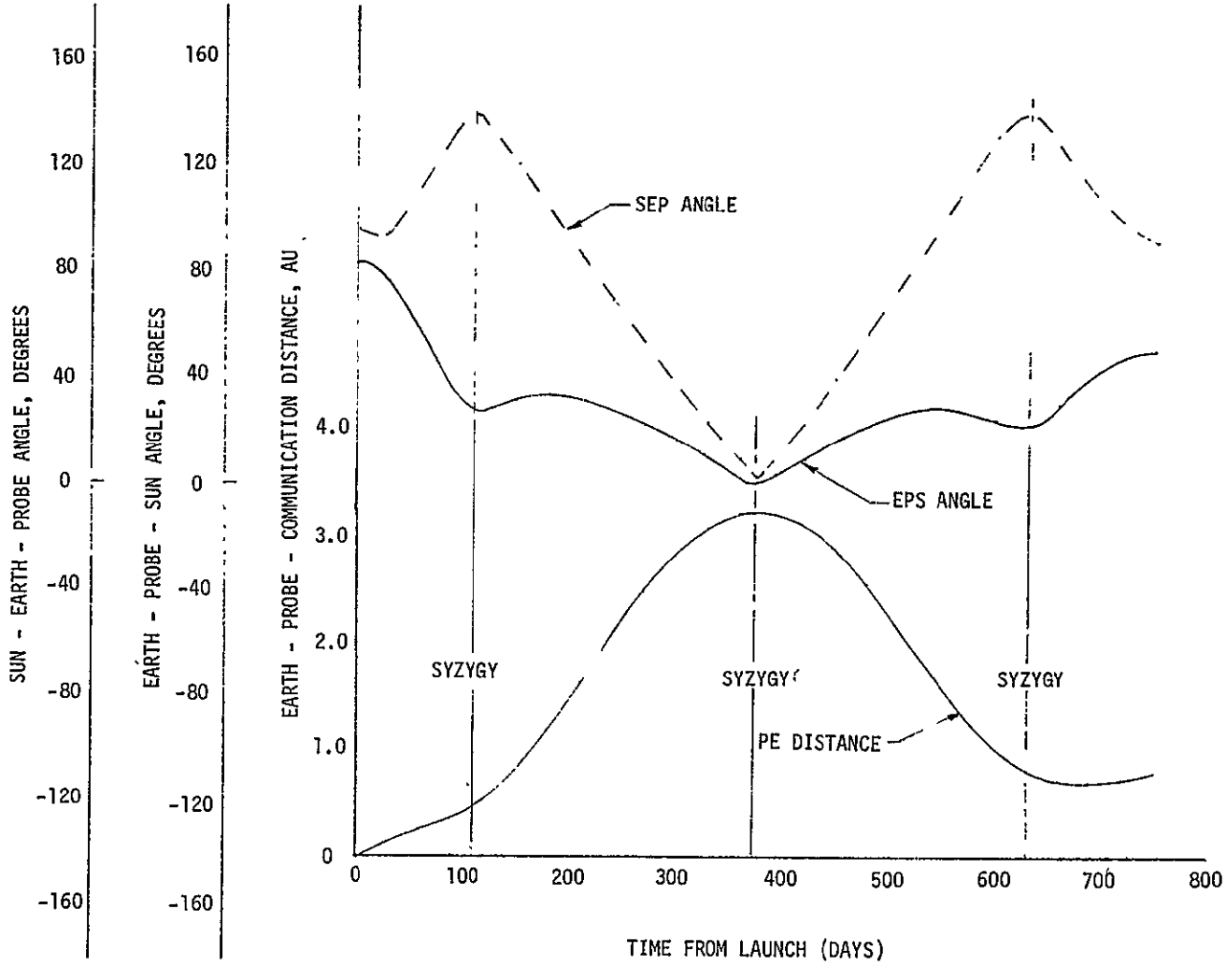

Figure B-6. Mission Data for Communications (Comet D'Arrest Rendezvous Mission)

SUMMARY - COMET ENCKE RENDEZVOUS

Orbital Elements

$a = 2.21$ AU
$e = 0.847$
$i = 12.4^{o}$
$\Omega = 334.7^{o}$
$\tilde{\omega} = \omega + \Omega = 159.9^{o}$
$\lambda^{*} = 159.9^{o}$
$T^{*} = 2444575$

Launch Vehicle Titan 3D/Centaur

SEP Stage (Optimal Pointing)

- Net Payload (Science) 481 KG
- Net Spacecraft 927 KG
- Injection Mass (M_o) 1859 KG
- Propellant Frac (M_p/M_o) 0.252
- Powerplant Frac (M_{pp}/M_o) 0.242
- Tank = 3% M_p
- α = 30 KG/KW
- Power = 15 KW
- I_{SP} = 3000 Sec

Earth Departure	March 7, 1978	V_∞ = 8.0 KM/SEC
Target Arrival	October 12, 1980	V_∞ = 0
Trip Time	950 Days	
Thrust Time	914 Days	

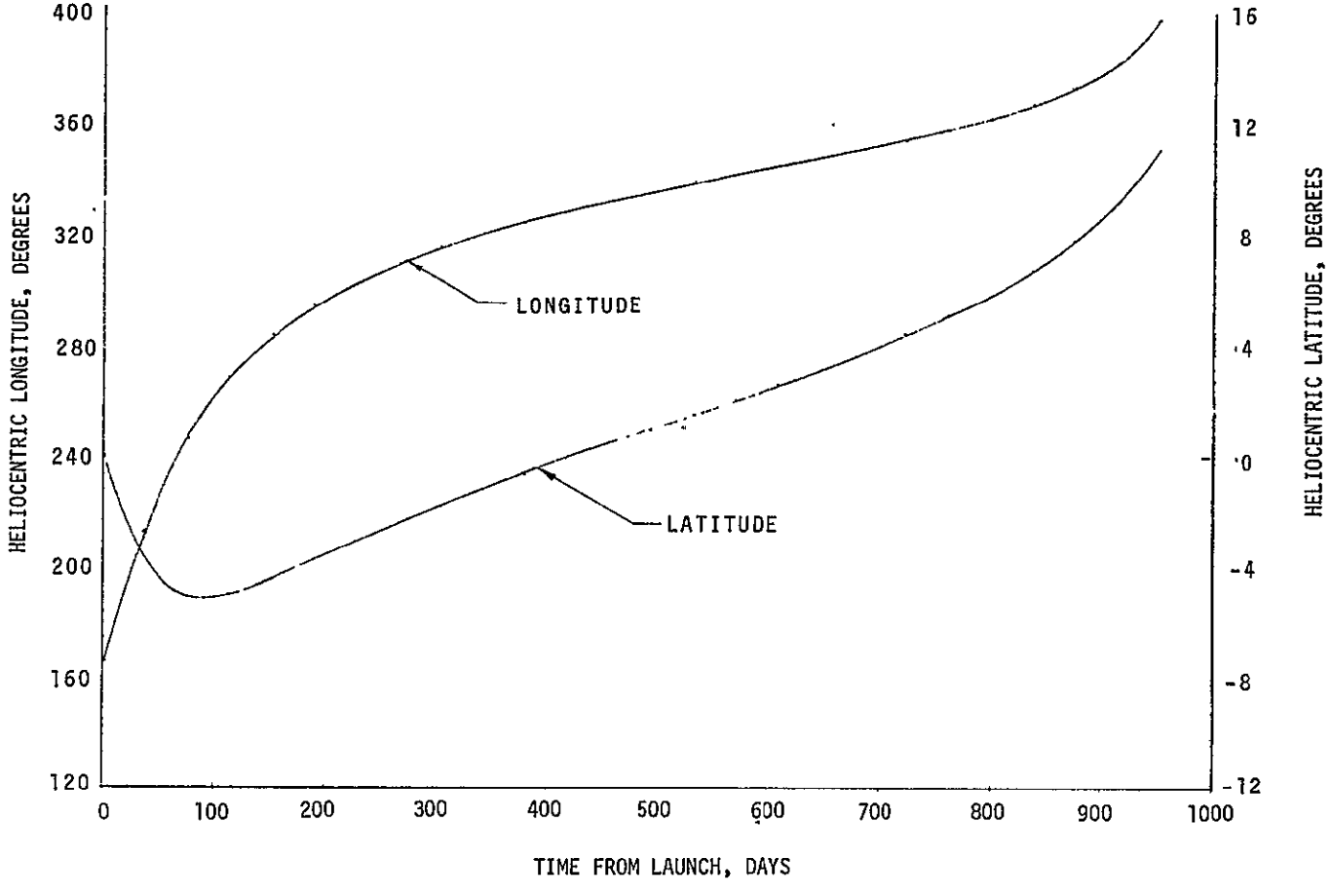

Figure B-7. Probe Position Angles
(Encke Rendezvous Mission)

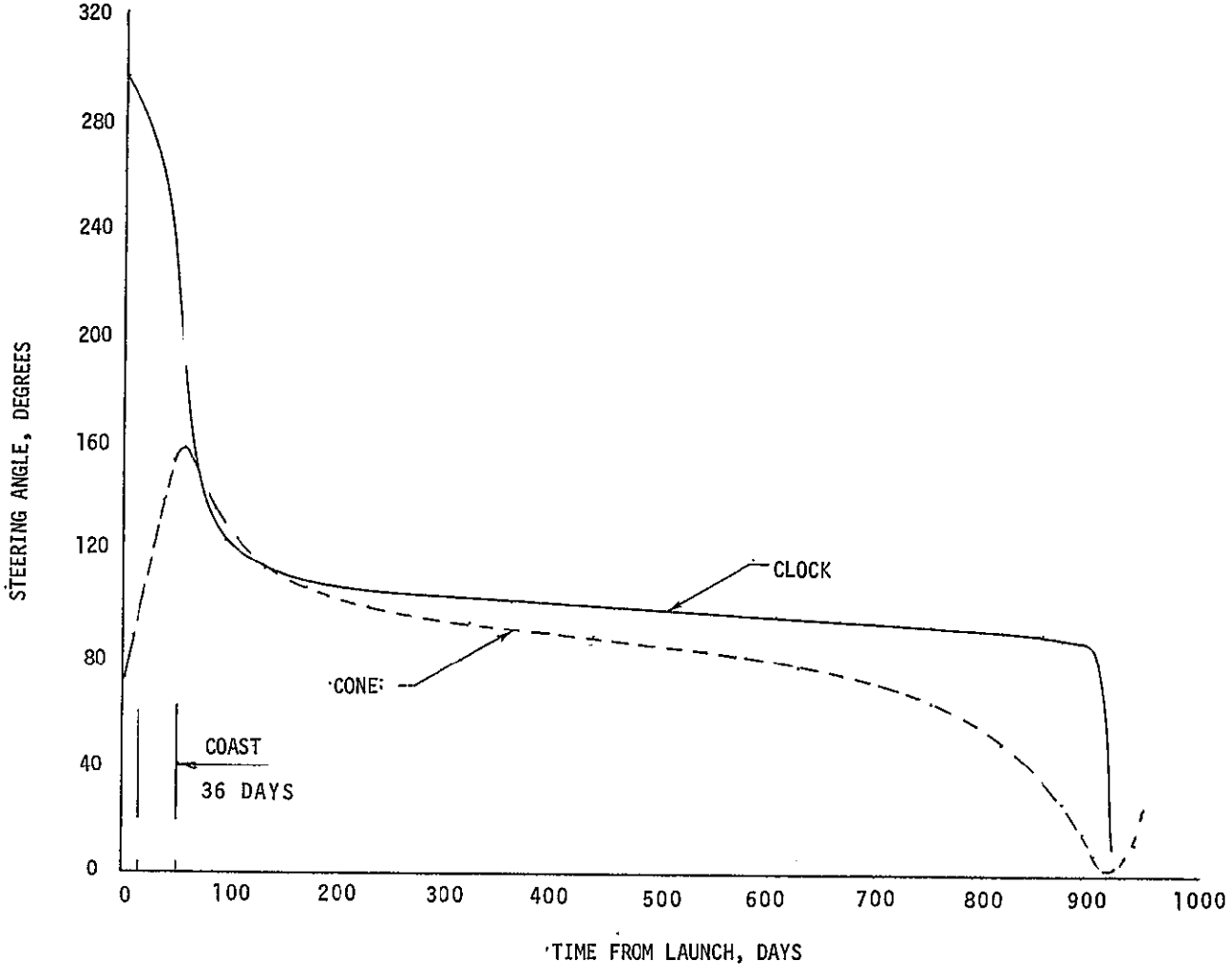

Figure B-8. Optimal Variable Steering Angle History (Encke Rendezvous Mission)

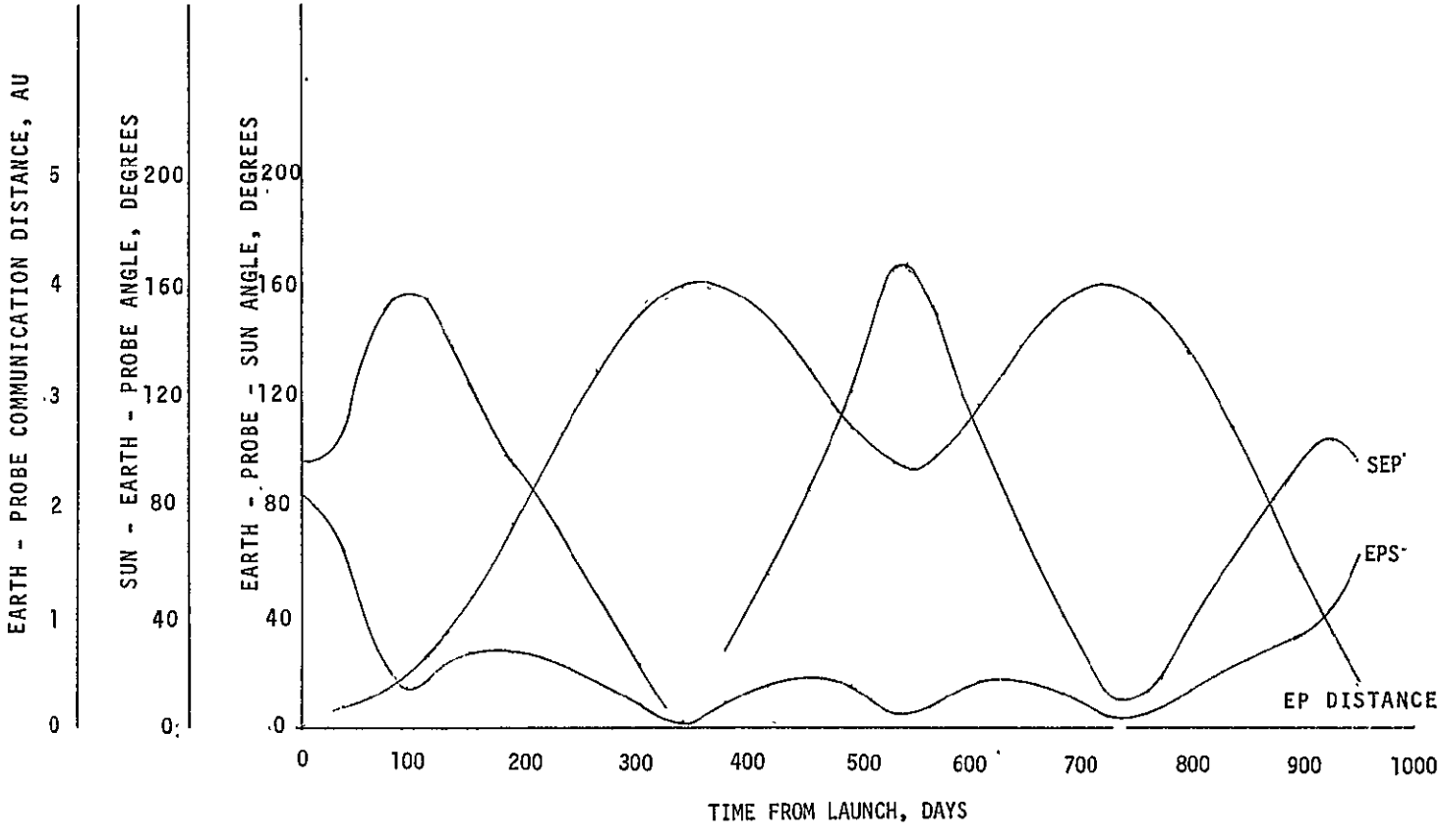

Figure B-9. Mission Data for Communications (Encke Rendezvous Mission)

SUMMARY - 45-DEGREE EXTRA-ECLIPTIC MISSION

Orbital Elements

$a = 1$ AU
$e = 0$
$i = 45^{o}$
$\Omega = 0^{o}$
$\tilde{\omega} = 0$
$\lambda^{*} = 0$

Launch Vehicle Titan 3D Centaur

SEP Stage (Optimal Pointing)

- Net Payload (Science) 70 KG
- Net Spacecraft 564 KG
- Injection Mass (M_o) 2143 KG
- Propellant Frac (M_p/M_o) 0.512
- Powerplant Frac (M_{pp}/M_o) 0.210
- Tank = 3% M_p
- α = 30 KG/KW
- Power = 15 KW
- I_{SP} = 3000 sec (η = 0.636)

Earth Departure	September 21, 1978	V_∞ = 7.5 KM/SEC
Target Arrival	August 25, 1980	V_∞ = 0
Trip Time	700 Days	
Thrust Time	521 Days	

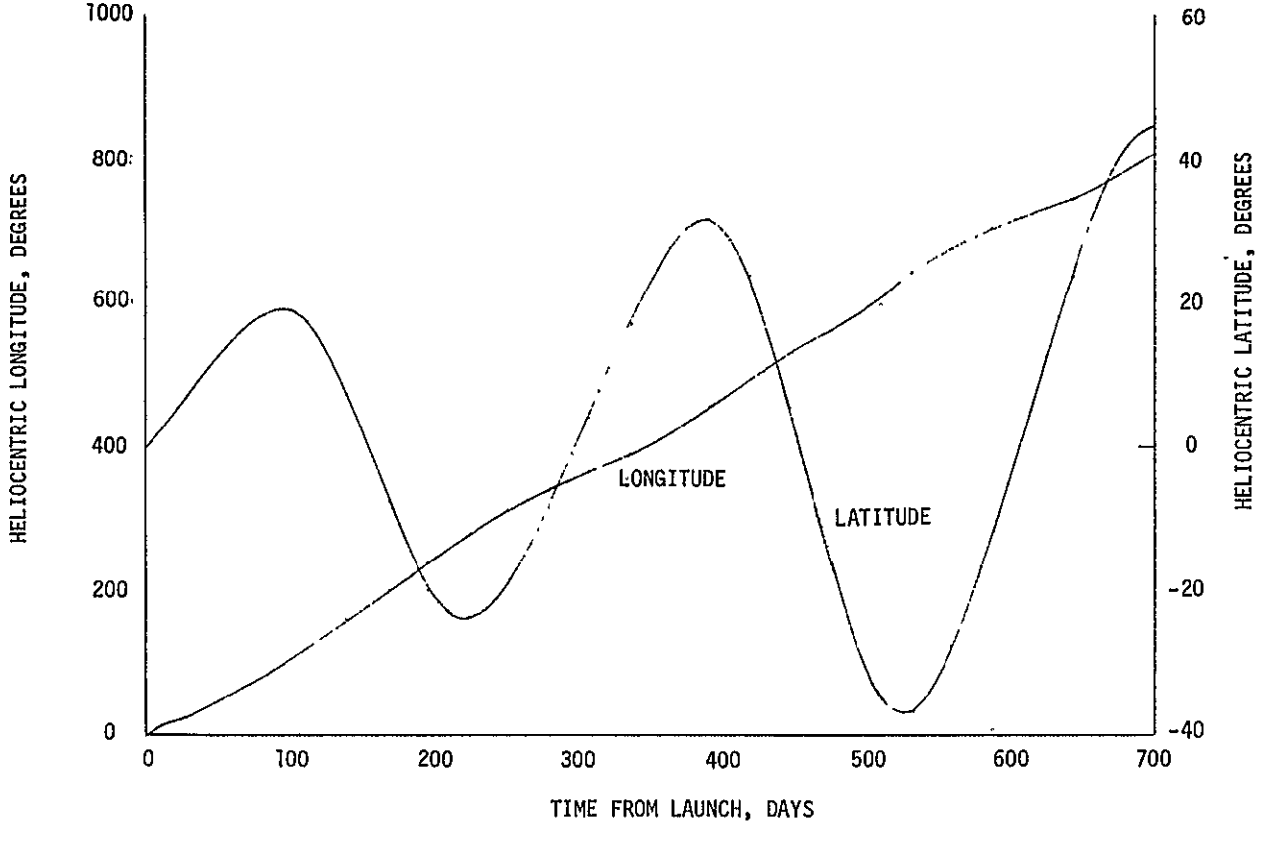

Figure B-10. Probe Position Angles
(45-Degree Extra-Ecliptic Mission)

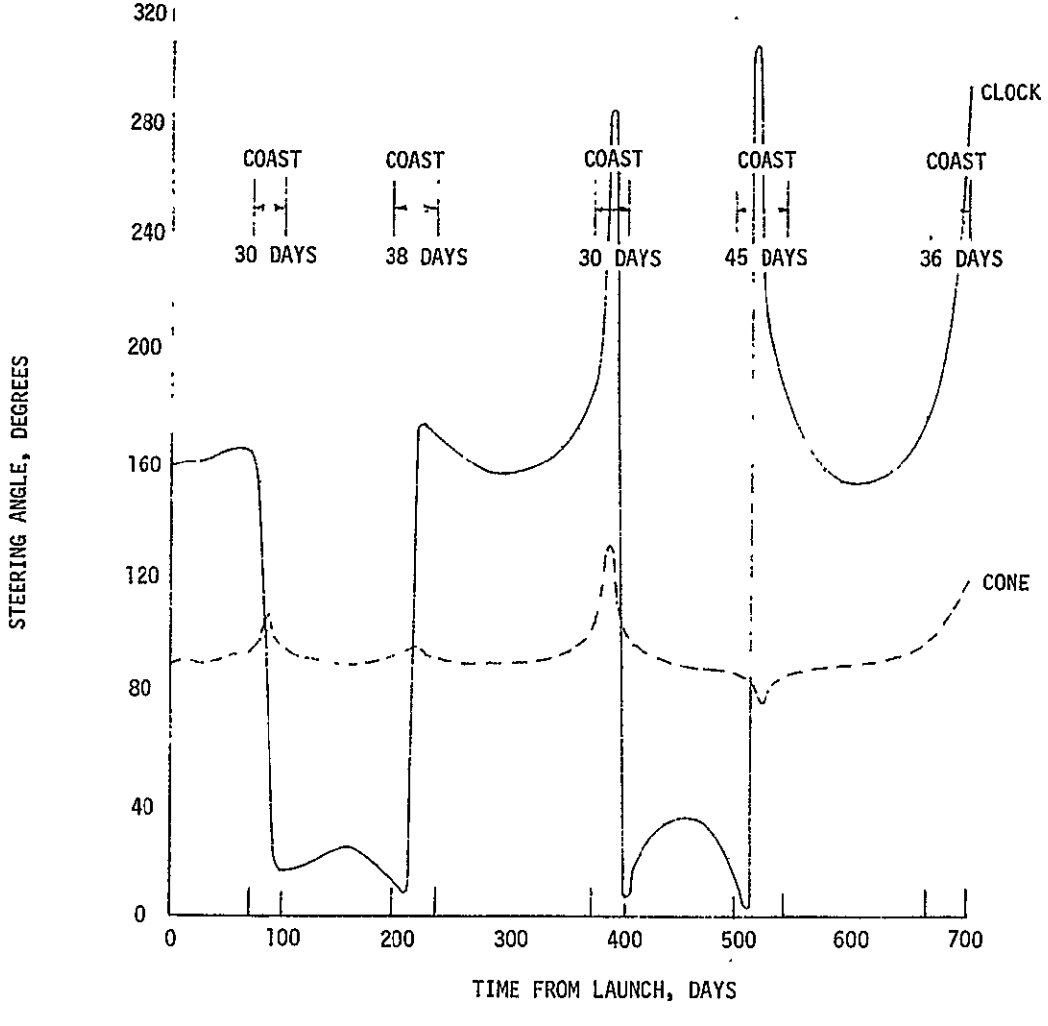

Figure B-11. Optimal Variable Steering Angle History (45-Degree Extra-Ecliptic Mission)

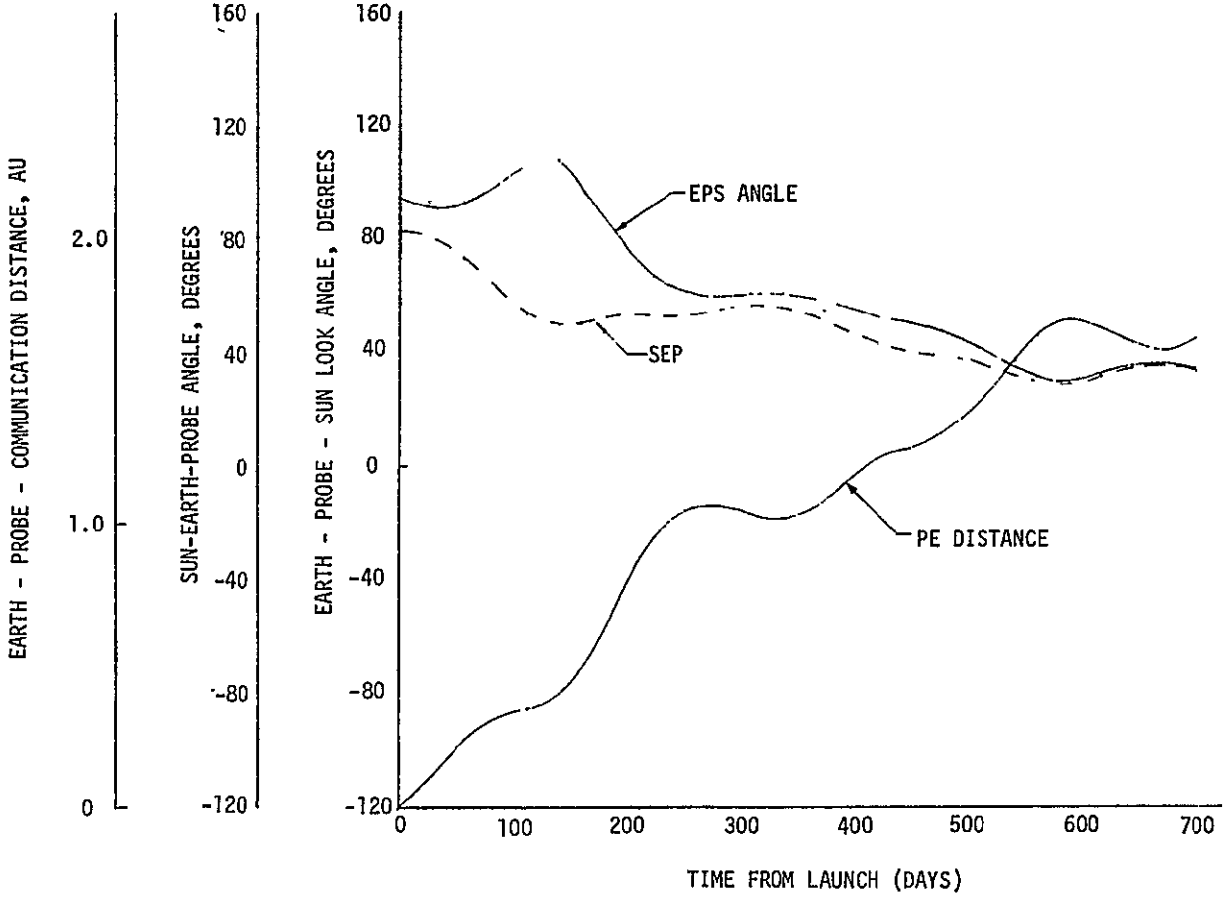

Figure B-12. Mission Data for Communications (45-Degree Extra-Ecliptic Mission)

SUMMARY - MERCURY ORBITER

Orbital Elements

$a = 0.3871$ AU
$e = 0.2056$
$i = 7.004^{o}$
$\Omega = 47.86^{o}$
$\omega = \omega + \Omega = 76.83^{o}$
$\lambda^{*} = 222.62^{o}$
$T^{*} = 2436935$

Launch Vehicle Titan 3D/Centaur

SEP Stage
(Optimal Pointing)

- Net Payload (Science) 126 KG
- Net Spacecraft 572 KG
- Injection Mass (M_o) 1859 KG
- Propellant Frac (M_p/M_o) 0.436
- Powerplant Frac (M_{pp}/M_o) 0.242
- Tank = 3% M_p
- α = 30 KG/KW
- Power = 15 KW
- I_{SP} = 3000 Sec

Earth Departure	June 9, 1980	V_∞ = 8.0 KM/SEC
Target Arrival	July 14, 1981	V_∞ = 0
Trip time***	402 Days	
Thrust Time	311 Days	

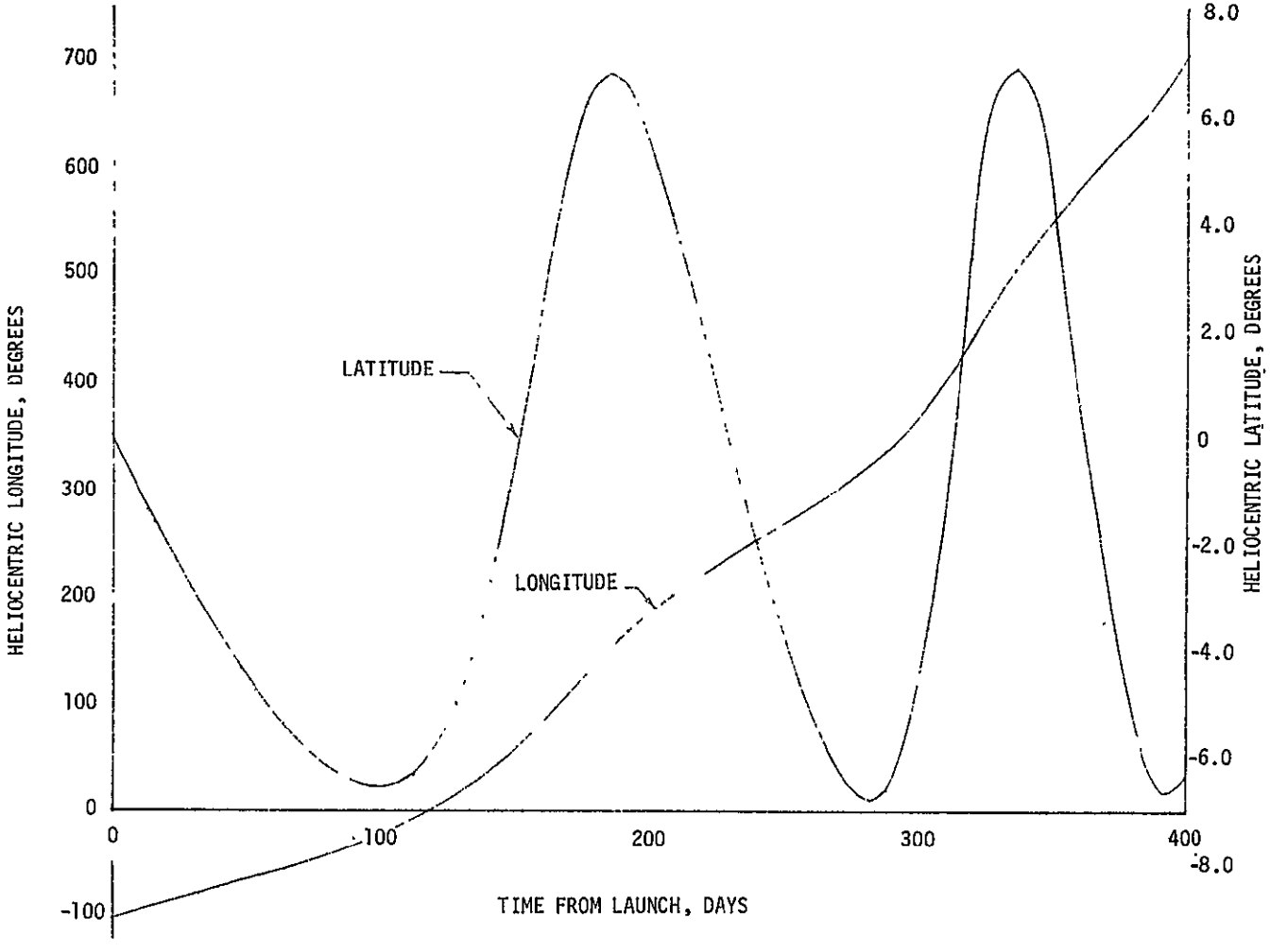

Figure B-13. Probe Position Angles
(Mercury Orbiter Mission)

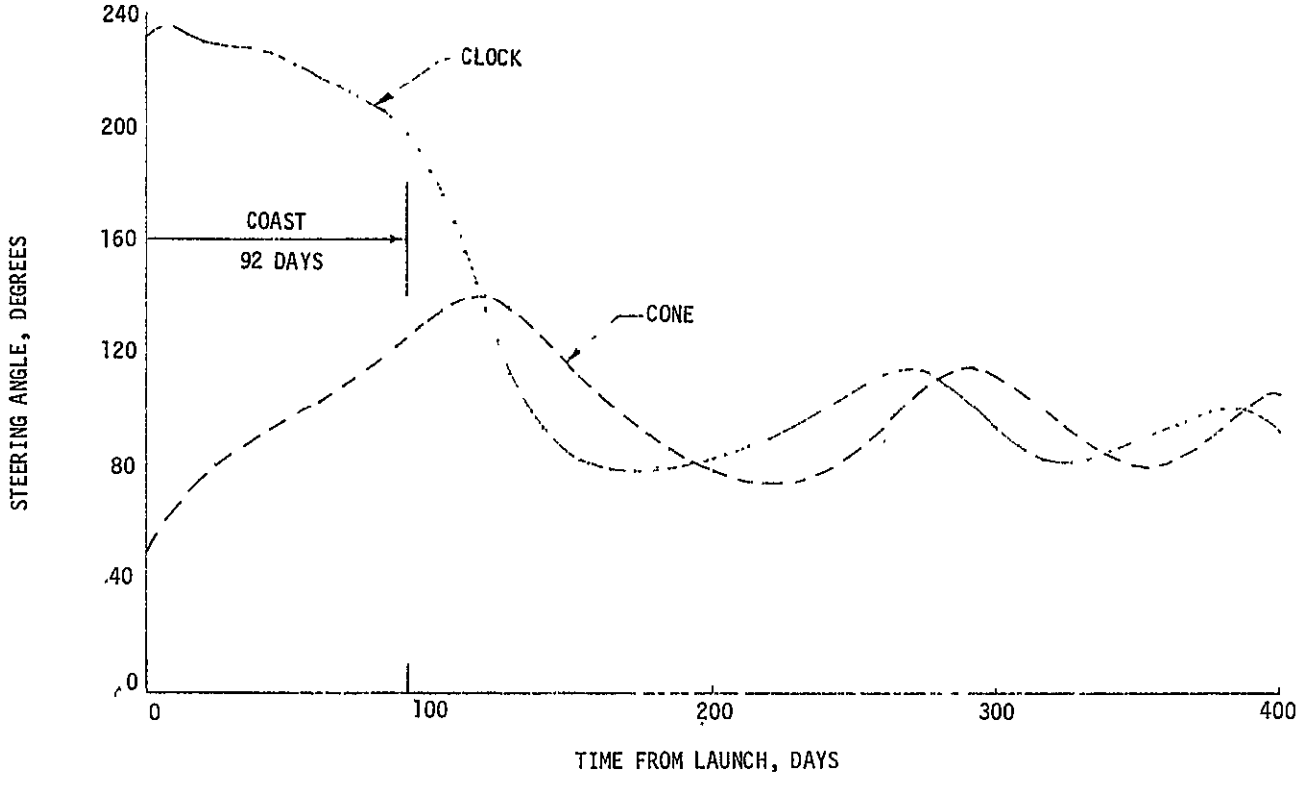

Figure B-14. Optimal Variable Steering Angle (Mercury Orbiter Mission)

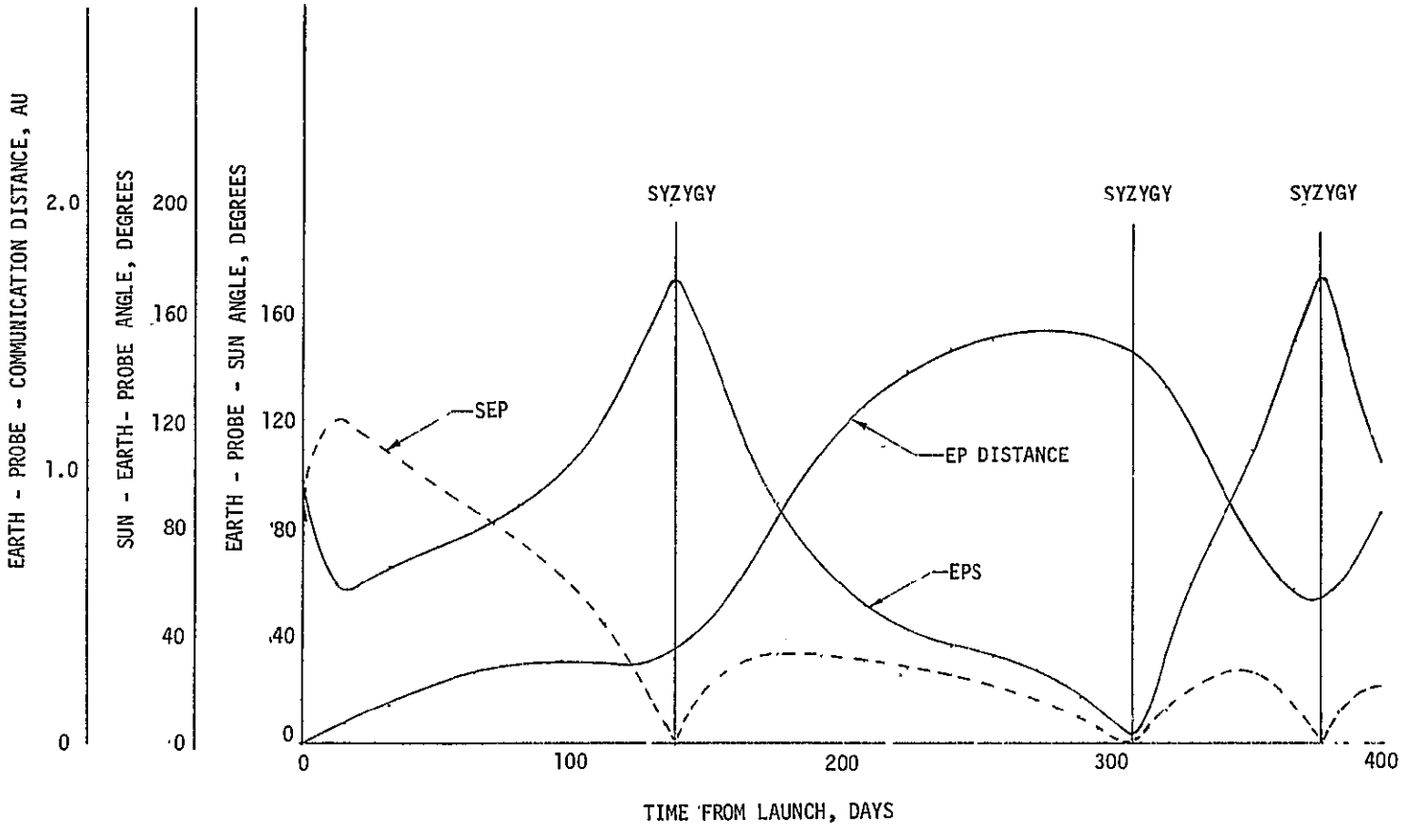

Figure B-15. Mission Data for Communications (Mercury Orbiter Mission)

SUMMARY - 0.1 AU SOLAR PROBE

Orbital Elements

$a = 0.511$ AU
$e = 0.8042$
$i = 0$
$\Omega = 0$
$\tilde{\omega} = \omega + \Omega = 184.145^{o}$

Launch Vehicle Titan 3D/Centaur

SEP Stage
(Circumferential Pointing)

- Net Payload (Science) 377 KG
- Net Spacecraft 823 KG
- Injection Mass (M_o) 1859 KG
- Propellant Frac (M_p/M_o) 0.306
- Power Plant Frac (M_{pp}/M_o) 0.242
- Tank = 3% M_p
- α = 30 KG/KW
- Power = 15 KW
- I_{SP} = 3000 Sec (η = 0.636)

Earth Departure	Open	V_∞ = 8.0 KM/SEC
Target Arrival	Open	
Trip Time	400 Days	
Thrust time	252 Days	

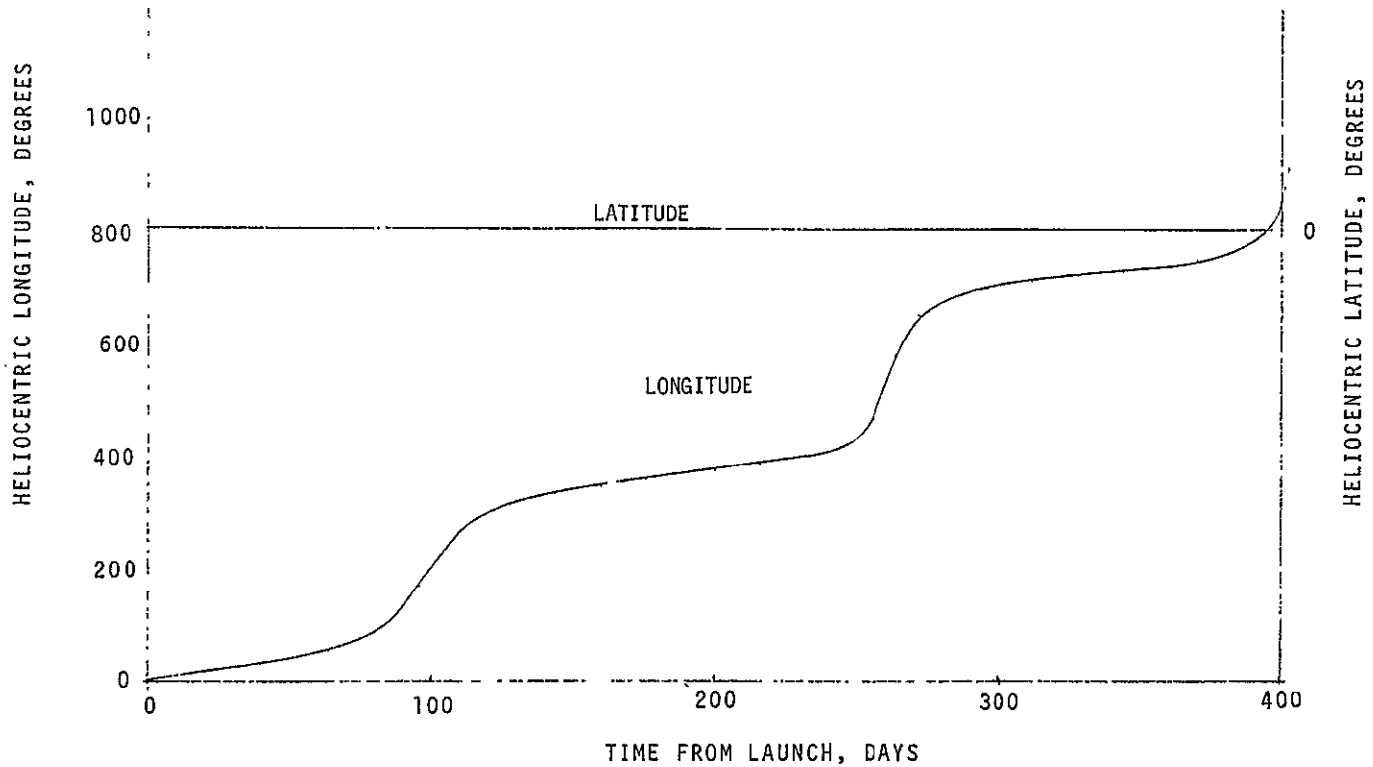

Figure B-16. Probe Position Angles
(0.1 AU Solar Probe)

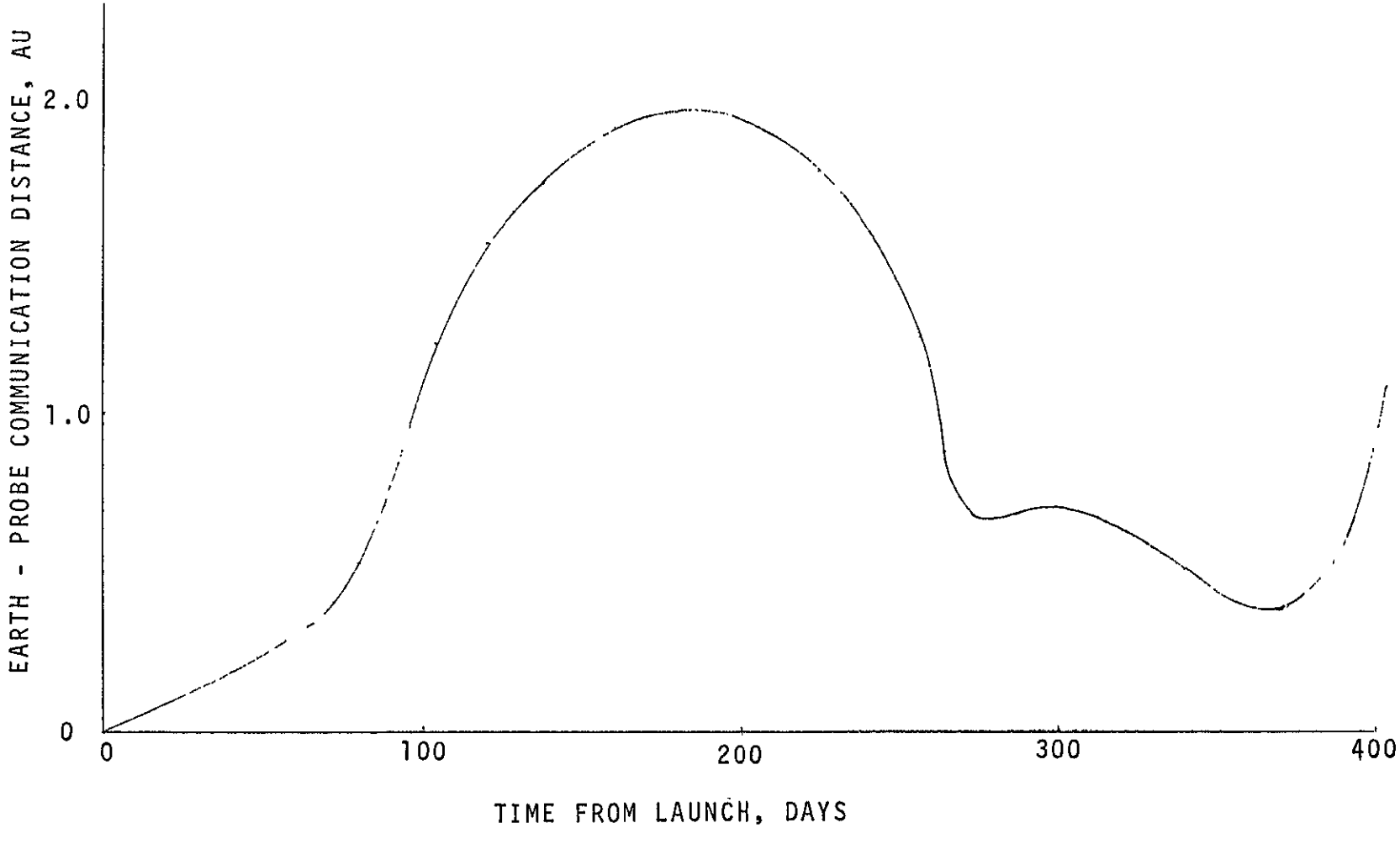

Figure B-17. Mission Data for Communications

APPENDIX C

ANALYSIS OF PAYLOAD LOSS DUE TO NON-OPTIMAL THRUST VECTOR ORIENTATION

Various thrust vector pointing options including optimal and non-optimal time varying, and optimal and non-optimal fixed pointing modes were investigated to determine their effect on payload capacity in the missions of interest. This was discussed in Section 5.8 of the Technical Report.

A simplified analytical approach was derived to permit coverage of the thrust vector pointing problem without obtaining a new integrated trajectory in each case which would be time consuming and costly. The payload loss due to non-optimal thrust vector steering can be expressed in good approximation by

$$\text{Relative loss in payload } L = \cong \frac{\mu_P}{\mu_L} \frac{\int_0^T a(t) \left[1 - \cos\left(\theta(t) - \theta_1\right)\right] dt}{\int_0^T a(t)\, dt}$$

where

μ_L = payload fraction

μ_P = propellant fraction

$a(t)$ = thrust acceleration magnitude

$\theta(t)$ = thrust pointing angle (cone angle)

} reference data from optimal time-varying thrust profile

θ_1 = assumed fixed pointing angle

This expression can be evaluated and optimum fixed angles θ_{1_o} be derived by simple algebraic manipulation of integrals of the known functions $a(t)$, $a(t) \cos \theta(t)$ and $a(t) \sin \theta(t)$.

The above expression for payload loss L is an explicit function of the parameter θ_1. The optimal fixed pointing angle at which the payload loss is minimized can therefore be readily derived:

$$\tan \theta_{1_{opt}} = \frac{\int_0^T a(t) \sin \theta(t)\, dt}{\int_0^T a(t) \cos \theta(t)\, dt}$$

The integrands in the numerator and demoninator terms are obtained from a given reference trajectory with optimal time-varying thrust angles. The integrals

$$A_1 = \int_0^T a(t) \sin \theta(t)\, dt, \quad A_2 = \int_0^T a(t) \cos \theta(t)\, dt$$

and $A_o = \int_0^T a(t)\, dt$ can be evaluated numerically or by an approximate graphical method. Using these terms we obtain the simple expressions

$$\theta_{1_{opt}} = \tan^{-1}(A_1/A_2)$$

$$L_{min} = \frac{\mu_P}{\mu_L}\left(1 - \frac{1}{A_o}\sqrt{A_1^2 + A_2^2}\right)$$

for the optimum fixed pointing angle and for the minimum payload loss that corresponds to $\theta_{1_{opt}}$

Figure C-1 shows the results obtained in a mission to D'Arrest. The net spacecraft mass deliverable with optimal variable thrust pointing is 810 kg. The optimum fixed-cone angle is 75 degrees yielding a net spacecraft mass of 775 kg. The graph shows payload loss as a function of selected thrust pointing angle (cone angle) as determined by the approximate analytical expression (dashed curve). The more exact values (solid curve) obtained by using the QUICKTOP trajectory program are also shown. The results are in excellent agreement at and near the optimum fixed-cone angle $\theta_{1_{opt}} = 75$ degrees. The approximation error is less than 2 percent over a 10-degree range of cone angles on both sides of the optimum but begins to increase rapidly beyond 15 degrees.

This method can be used readily to evaluate other non-optimum thrust pointing modes such as constrained thrust angle variations by body reorientation, or discrete changes of thrust angle. For example, if the

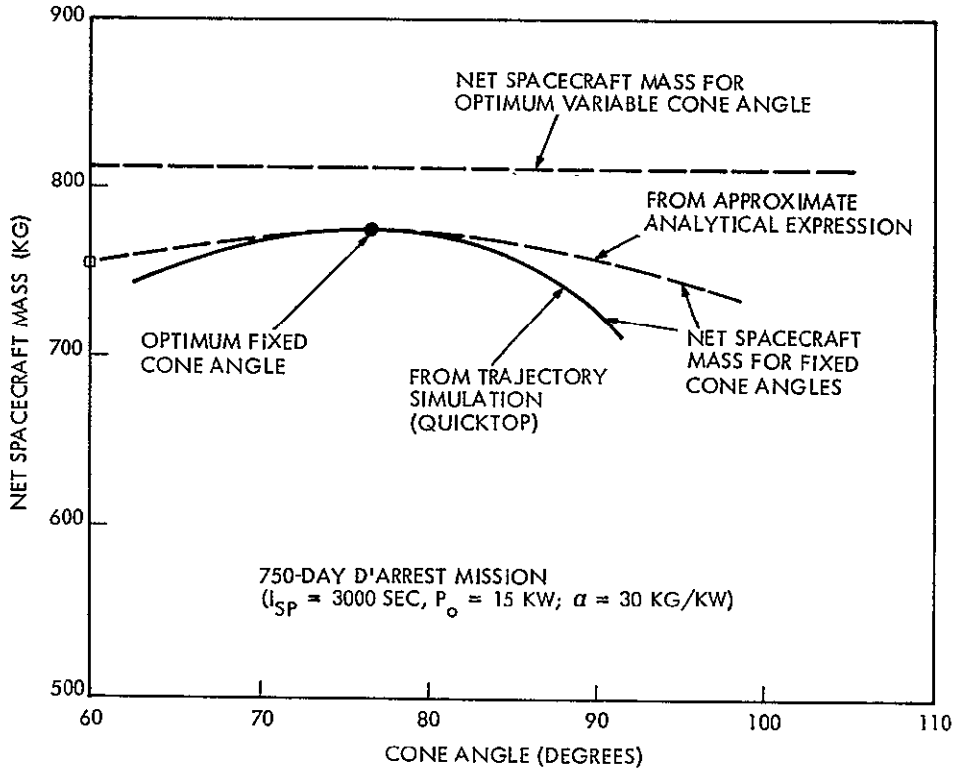

Figure C-1. Comparison of Approximate and Accurate Methods for Determining Payload Loss due to Non-Optimal Thrust Pointing

non-optimal pointing angle θ_1 is made time-varying such that $\theta_1(t) = 1/2\theta(t)$ (i. e., equal to half the optimal pointing angle) the payload loss is only about one quarter of that resulting from optimum fixed pointing because of the cosine effect involved, as can be easily seen from the first equation above.

This method remains applicable in the three-dimensional case because out-of-plane thrust angle variations can be accomplished by rotating the entire spacecraft through the appropriate clock angle. This has no effect on cone angle pointing deficiencies, hence the above approximation involving the angle difference $\theta(t) - \theta_1$ remain unchanged.

APPENDIX D

UTILIZATION OF EARTH SWINGBY

A significant improvement of solar-electric spacecraft performance in interplanetary missions can be achieved by using an indirect mission mode that includes an earth swingby maneuver. This unconventional mission profile permits accumulation of electric propulsion energy during a six-month time interval in which the spacecraft maintains a 1 AU radial distance from the sun. This mission phase is followed by the earth encounter. As a result of gravity perturbation the velocity increment gained prior to the encounter is converted during the swingby phase into a velocity increment that significantly increases the energy of the subsequent transfer trajectory. In addition to exploiting solar-electric energy at a favorable solar distance, this mission mode releases the accumulated velocity increment in a quasi-impulsive manner at a solar radius where aphelion changes in outbound missions or perihelion changes in inbound missions are performed most effectively. The swingby maneuver can also be used to yield large changes of the departure angle in or out of the ecliptic plane that would be much more costly to achieve in a direct mission mode. In its application to outer planet missions the earth swingby mode can be compared to more conventional indirect mission modes which make effective use of solar-electric propulsion by initially swinging inside the earth's orbit. This concept has been discussed in a recent paper by H. F. Meissinger*

Two types of earth swingby mission profiles have been considered. The first type uses a pre-encounter trajectory that is inclined relative to the ecliptic plane. By thrusting out of plane the inclination prior to earth encounter and hence the swingby velocity is increased. The second type remains in the ecliptic prior to encounter; in-plane thrusting increases the relative encounter velocity in this mode.

*"Earth Swingby - a Novel Approach to Interplanetary Missions Using Electric Propulsion" by H. F. Meissinger, AIAA Paper No. 70-1117, presented at the 8th Annual Electric Propulsion Conference, Stanford, Aug. 21 - Sept. 2, 1970.

Figure D-1 illustrates the first (out of plane) type of swingby mission profile for an outer planet mission. Figure D-2 shows a variety of missions that can be achieved by this mode. Figure D-3 shows applications of the second (in plane) type of mission profile applied to in-ecliptic and out-of-ecliptic probes.

The effective performance gain achieved by earth swingby six months after launch is shown in Figure D-4. The diagram at the left shows increase in departure energy C_3 which results from a velocity increment of 2, 3, and 4 km/sec due to low thrust applied prior to earth encounter. The effective increase in booster performance is shown at the right for Titan 3D/Centaur, Titan 3C/Burner 2, and Atlas/Centaur/Burner 2. The performance improvement achieved by this technique is equivalent to an injected weight increase of about 30 percent in the hyperbolic departure velocity range of 2 to 4 km/sec (see Figure D-4).

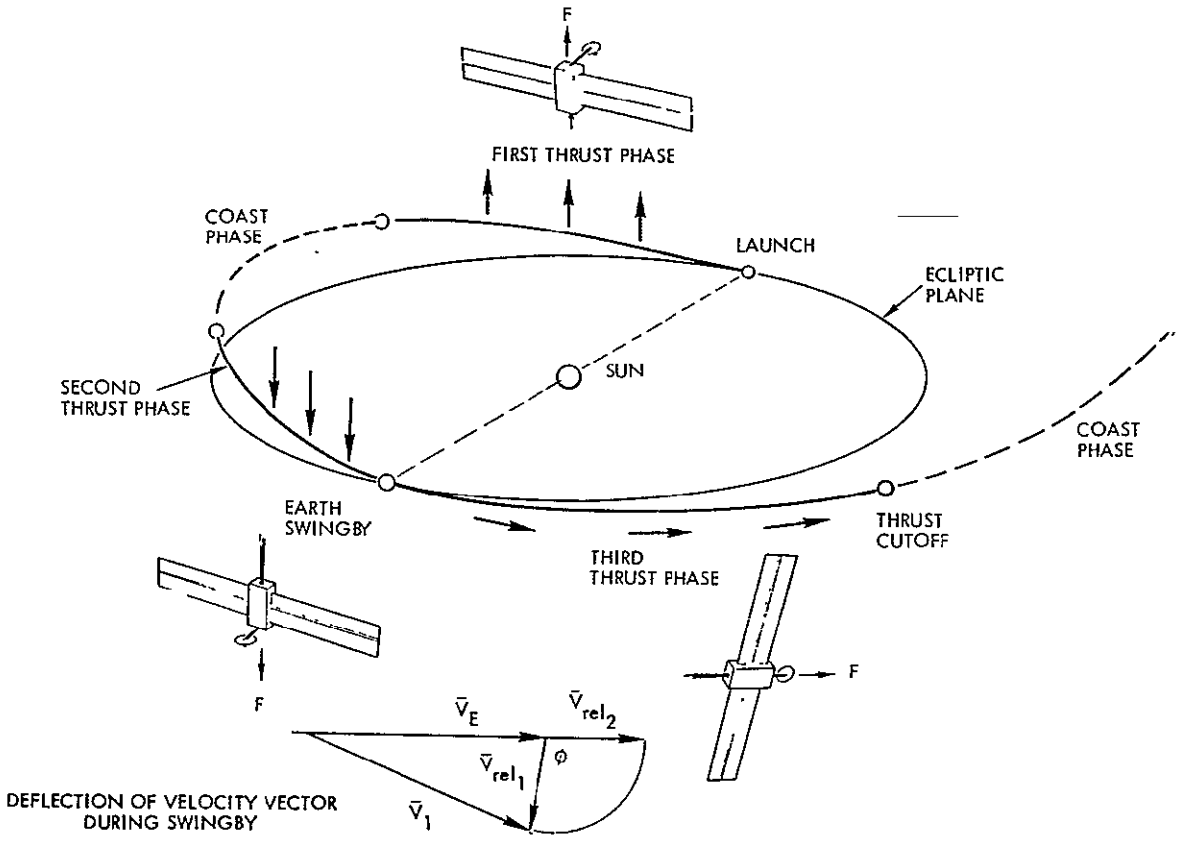

Figure D-1. Outer Planet Mission with Earth Swingby: Mission Profile and Thrust Pointing Requirements

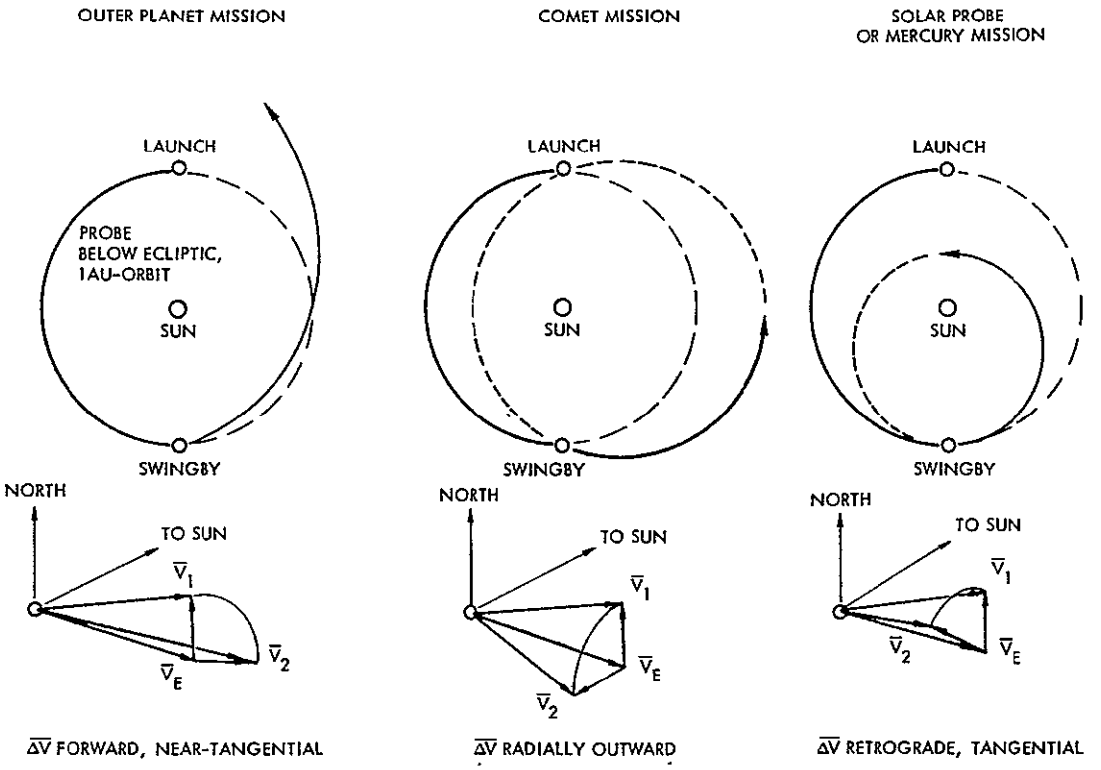

Figure D-2. Multiple Mission Options Available Through Swingby Maneuver

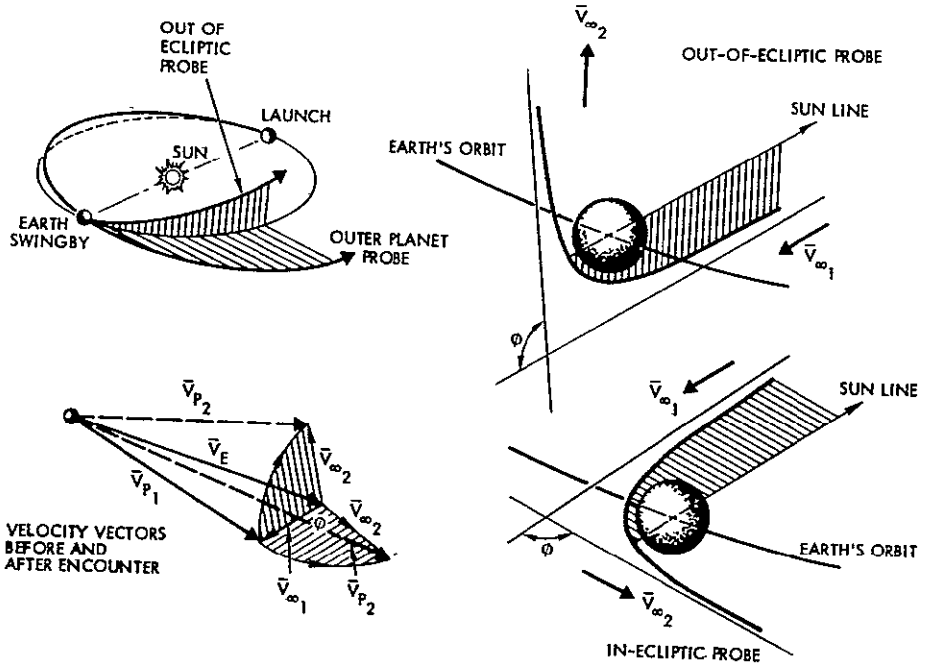

Figure D-3. Branch Trajectories to Different Destinations Controlled by Different Encounter Geometries

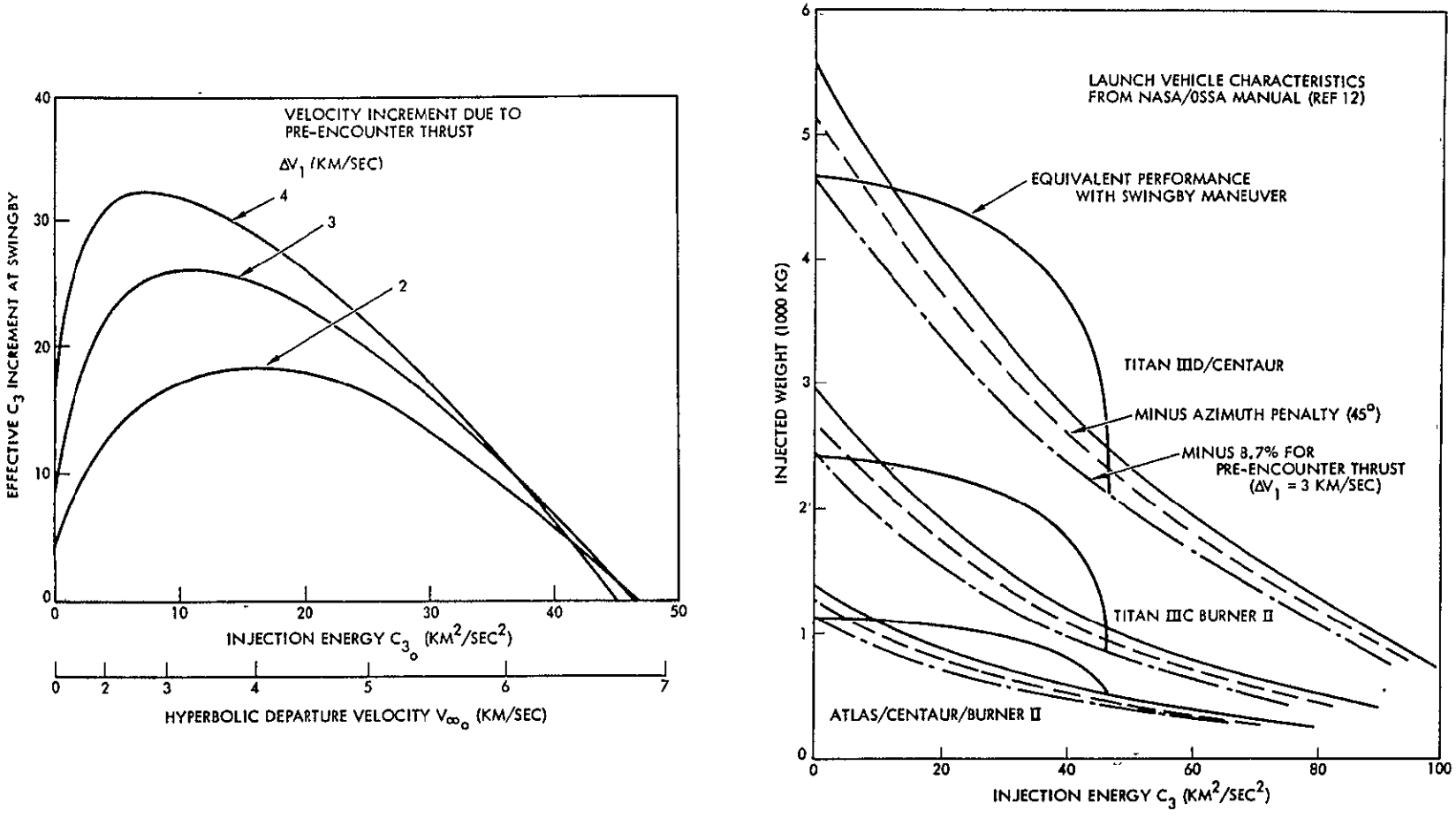

Figure D-4. Increase of Equivalent Injection Energy by Earth Swingby Maneuver

This performance improvement would not be required for Titan 3D/Centaur in the single launch mode, but can be very useful in the dual launch mode. It would also be useful with a lower performance booster such as Titan 3D/Burner 2.

Earth swingby applied to the multi-mission electric stage has the principal advantage of permitting the targeting of two tandem-launched vehicles to different destinations. This is achieved by using dissimilar three-dimensional earth encounter conditions such that the trajectories are deflected in different directions. Figure D-3 illustrates dual-launch trajectories that lie in the ecliptic plane prior to encounter and are separated into an out-of-ecliptic and in-ecliptic branch at swingby. Launch in the ecliptic plane permits pairing of an out-of-ecliptic mission with missions in the ecliptic making an easterly launch azimuth off Cape Kennedy compatible with both mission types. The azimuth penalty of a near-polar launch which would normally be required for out-of-ecliptic missions is thus avoided.

APPENDIX E

ADDITIONAL MISSION CHARACTERISTICS OF A REPRESENTATIVE COMET RENDEZVOUS (ENCKE 1980)

E. 1 MISSION PROFILE SELECTION CRITERIA

Figure E-1 shows representative Encke rendezvous trajectories projected into the ecliptic plane with arrival times at the comet 100 and 50 days before perihelion and at perihelion passage. The flight times are 900, 950 and 1000 days, respectively. These trajectories were briefly discussed in Section 5. 7 of the Technical Report, and mission profile data of the selected nominal 950-day trajectory were presented in that section and in Appendix B. Additional characteristics of the Encke mission are discussed below to illustrate mission profile selection criteria and operating modes in a representative comet rendezvous.

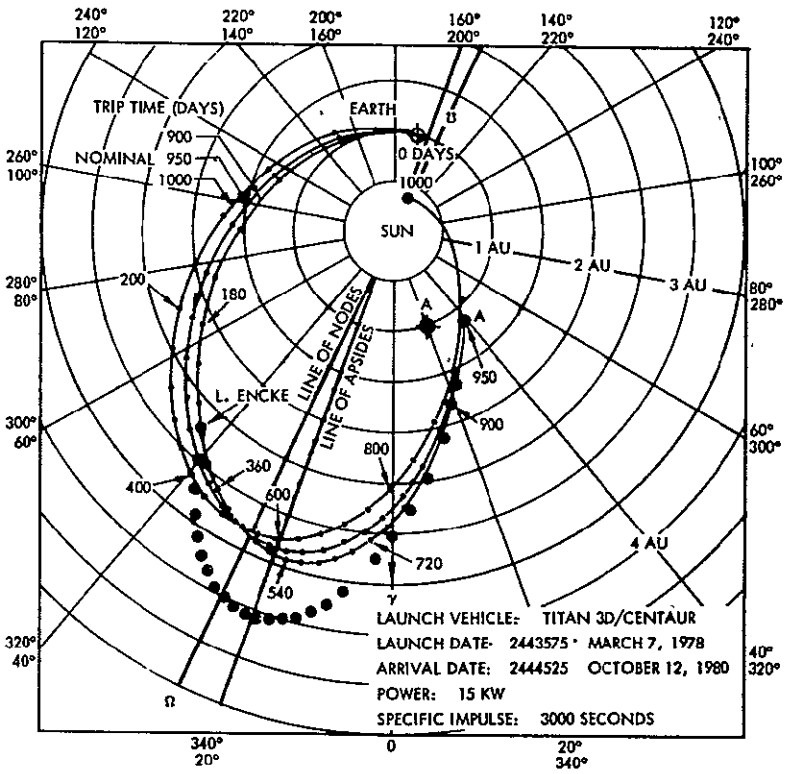

Figure E-1. Sample Trajectory Profiles Projected into Ecliptic Plane

The cases shown bracket mission times of practical interest for the electric stage. We note that in the 950-day sample trajectory nearly continuous thrusting is required from earth departure to comet arrival, with the exception of a 36-day coast period early in the mission, Figure E-2. Other mission profiles are possible where the thrust time or the mission time are shortened through choice of a higher departure velocity and/or higher thrust acceleration with the result of a reduction in payload mass.* The tradeoff is between shortened thrust time and flight time which increases mission success probability, and greater payload capacity and thus, scientific mission yield.

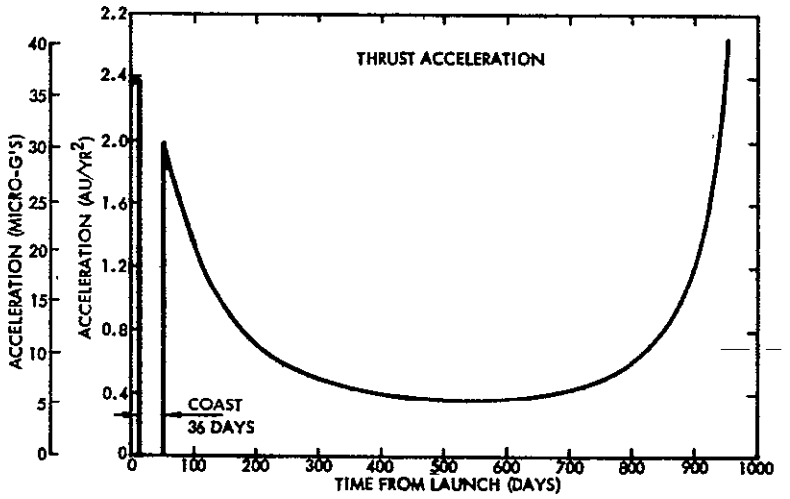

Figure E-2. Thrust Acceleration Profile for 950-day Mission

Payload variations resulting from changes in departure and arrival dates are shown in Figure E-3 for missions with flight times in the range of 850 to 1000 days. Flight times are indicated by diagonal lines. The ten data points indicated in this mission map give the optimum net spacecraft mass based on an initial thrust power of 15 kw and net spacecraft mass contours are derived from these points.

---

* Horsewood, J. L., Mann, F. I., and Flanagan, P. F., "Solar Electric Performance Data for Extra-Ecliptic and Solar Probes and Ceres, D'Arrest, and Encke Rendezvous Missions," Analytical Mechanics Associates, Inc., Report No. 70-47, dated December 1970.

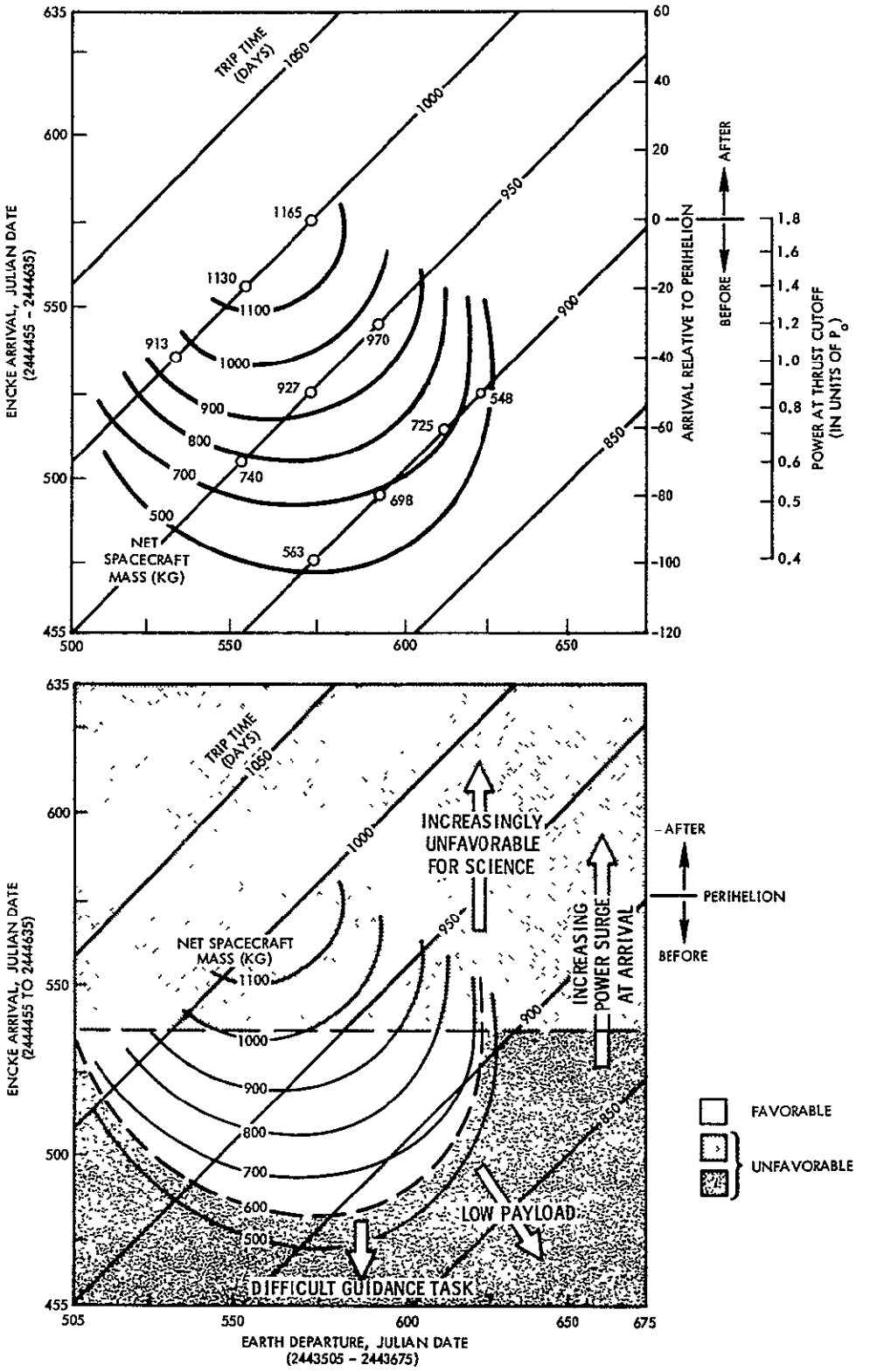

Figure E-3. Sample Encke Rendezvous Mission Map (Titan 3D/Centaur, P_o = 15 kw, I_{sp} = 3000 sec, α = 30 kg/kw)

The mission map is used to delineate constraints on the arrival and departure dates that are dictated by scientific objectives, spacecraft design requirements and other performance criteria. The scale on the right indicates the date of arrival relative to Encke's perihelion passage. The scientific interest in an early arrival at the comet (lower half of the map) must be weighed against practical constraints such as:

- Reduced payload capacity
- Increased communication range to earth
- Greater difficulty in achieving effective terminal guidance.

Terminal guidance is made more difficult in the case of an early rendezvous since much less thrust power is available for terminal maneuvers, and on-board acquisition of the comet for terminal navigation fixes may only be possible a short time before rendezvous, owing to the faintness of the comet at solar distances greater than 2.5 AU. Regions of favorable and unfavorable launch and arrival dates based on these criteria are outlined in the lower portion of Figure E-3.

The mission map also indicates the region that would be preferred from the standpoint of electric propulsion system design. A second scale at the right margin shows the peak power available for propulsion at the time of arrival, expressed non-dimensionally in units of initial power. A large surge in power occurring prior to arrival, as illustrated in the sample thrust power profiles, Figure E-4, reflects in a rapid increase in the number of operating thrusters at that time. This would introduce complications in propulsion module design and affect reliability characteristics.

Table E-1 summarizes principal parameters of three mission profiles to illustrate the interplay between potentially conflicting requirements of scientific mission effectiveness and propulsion system design. The shortest of the three missions, Mission Profile 1, arrives for an early rendezvous 80 days before perihelion passage, which is desirable from a standpoint of extended comet observation during the critical period. It also requires the shortest thruster time and thus gives a favorable propulsion module reliability, but it delivers the smallest

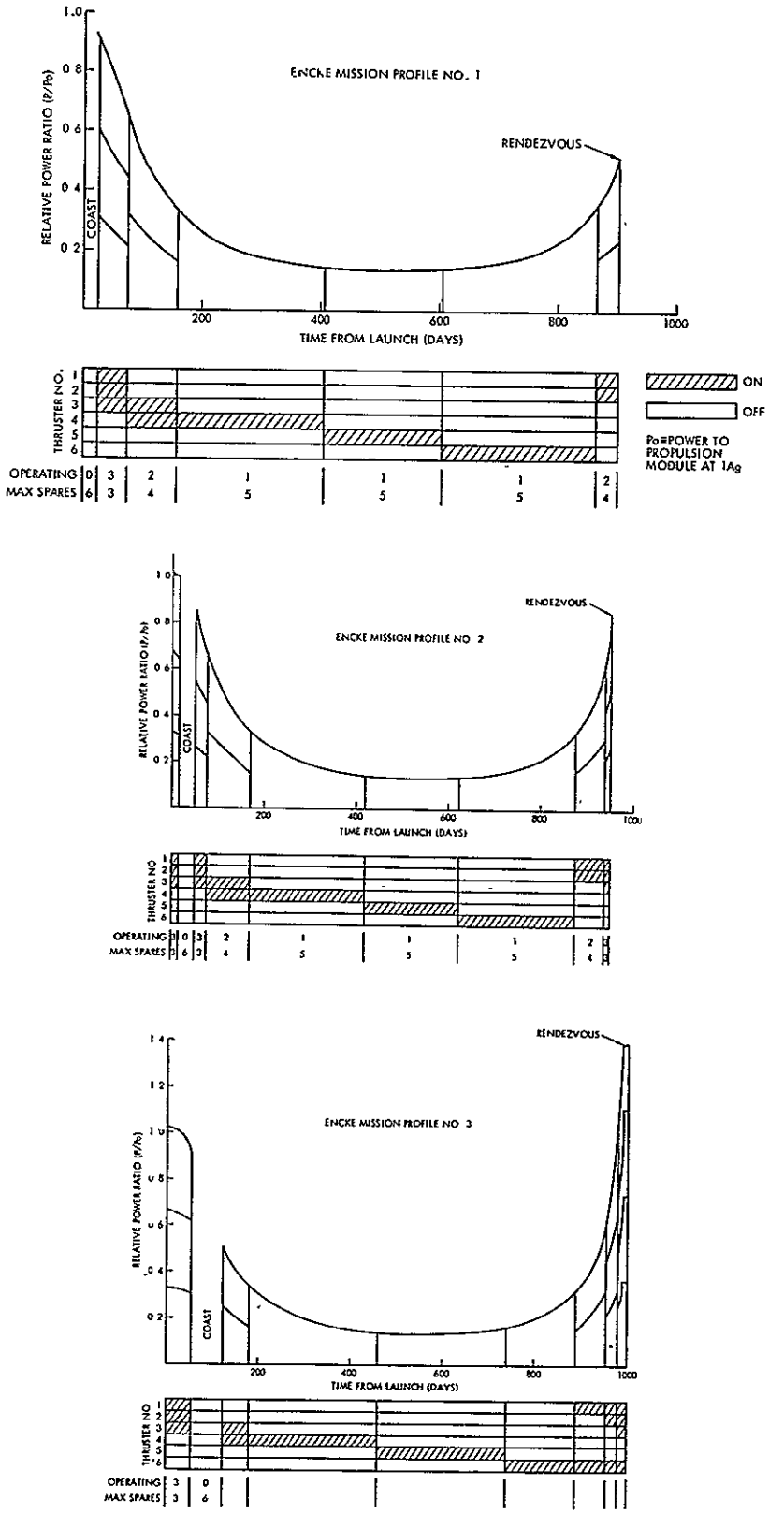

Figure E-4. Sample Mission Profiles for Encke Rendezvous Mission

payload of the three cases considered. The opposite is true in the case of Mission Profile 3. Thus, for the three missions evaluated in this example, it appears that Mission Profile 2, the 950-day mission, presents the best compromise between propulsion and power system requirements and desirable payload characteristics.

Table E-1. Typical Science-Propulsion System Tradeoff Parameters*

MISSION PROFILE NO.	TOTAL MISSION TIME TO RENDEZVOUS	TOTAL PROPULSION BURN TIME	SOLAR DISTANCE AT RENDEZVOUS	TIME BEFORE PERIHELION AT RENDEZVOUS	NET SPACECRAFT MASS	THRUST LEVEL AT RENDEZVOUS	PROPULSION MODULE RELIABILITY
1	900 Days	890 Days	1.6 AU	80 Days	698 KG	0.06 lb_f	0.965
2	950 Days	915 Days	1.1 AU	50 Days	927 KG	0.10 lb_f	0.96
3	1000 Days	970 Days	0.6 AU	20 Days	1130 KG	0.16 lb_f	0.722

*Assumes P_o = 12 kw, I_{sp} = 3000 sec, six thrusters, four beam and accelerator power processors, six multiple output power processors.

E. 2 OPERATIONS IN THE VICINITY OF THE COMET

Mapping of the comet's coma and tail is envisioned to be performed in a criss-cross pattern that makes use of the maneuver capacity provided by the electric propulsion system (Figure E-5). Since rendezvous occurs at about 1 AU and solar distance keeps decreasing in the immediate post-rendezvous phase a large amount of propulsion power will be available giving a thrust acceleration of 50 micro-g or more, i. e., velocity increments of at least 40 m/sec per day. The maneuvers for a criss-cross mapping pattern are intermittent so that interaction with delicate particles and fields measurements is avoided during most of this exploration.

When mapped in relative coordinates the coast trajectories of the spacecraft tend to curve away from a straight line in a direction toward or opposite to the comet's motion depending on whether they are aimed inward or outward, forming segments of epicycloidal arcs as shown in Figure E-6. This facilitates back and forth traverses of the comet tail

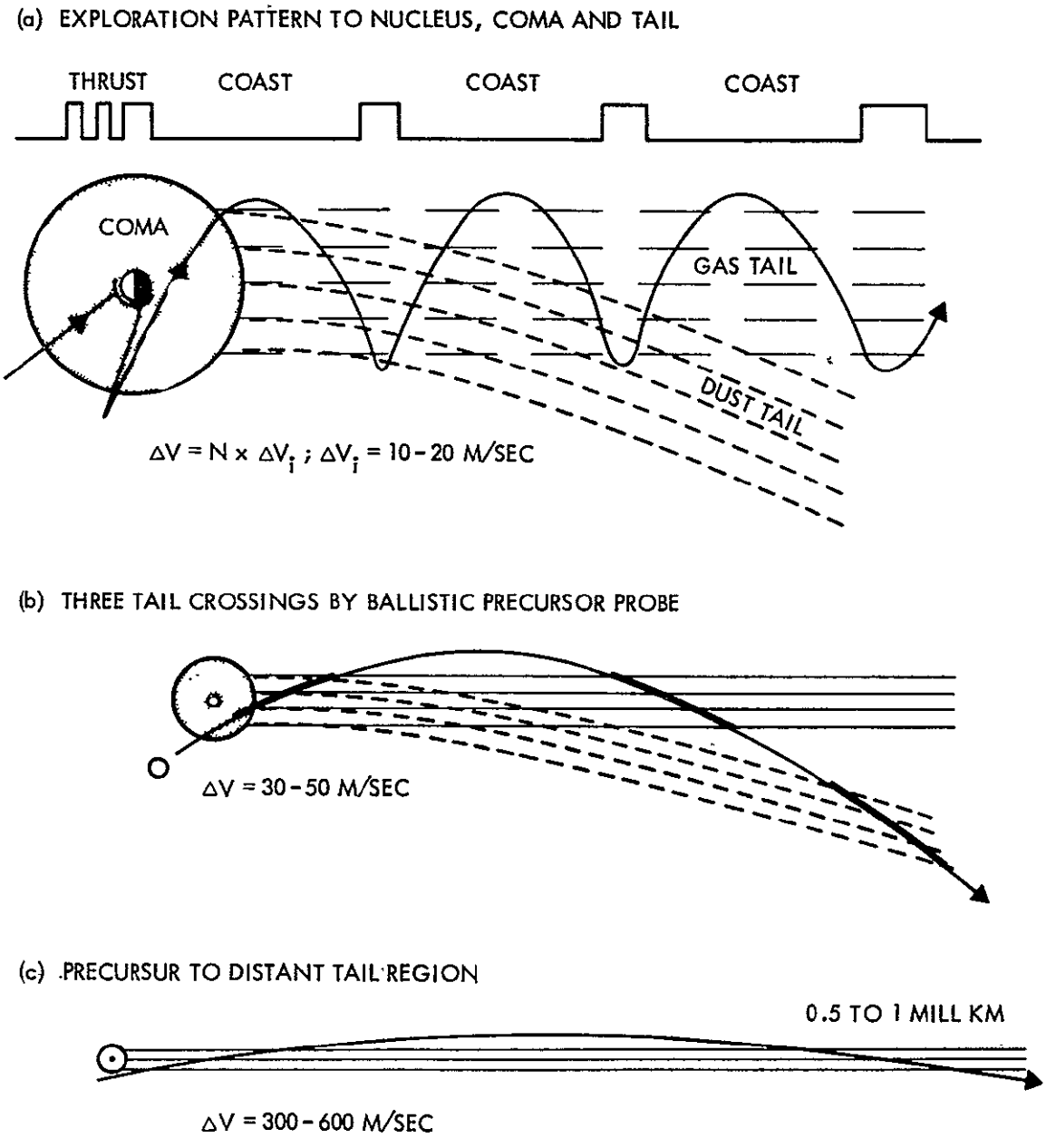

Figure E-5. Samples of Relative Trajectories for Comet Exploration

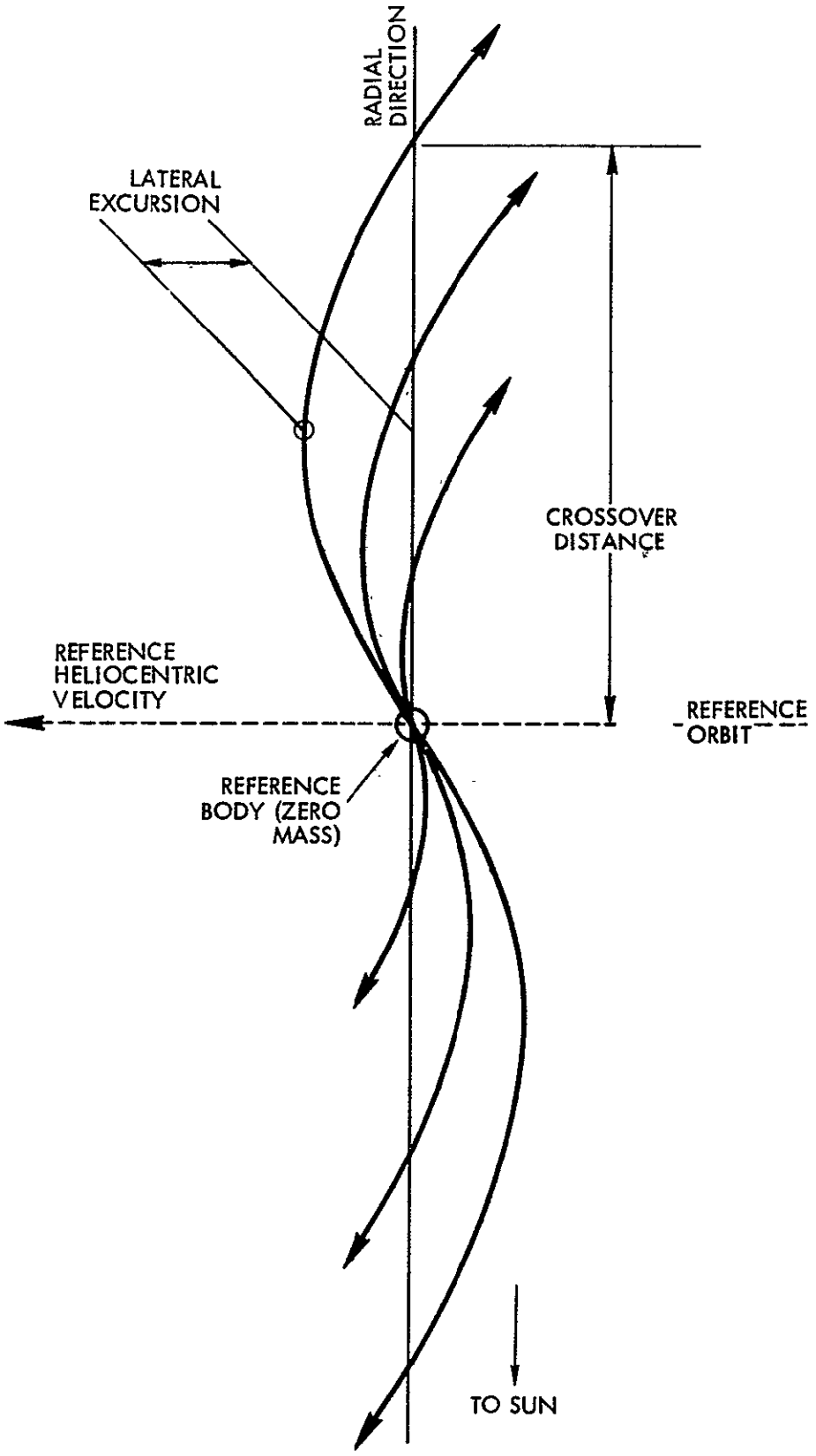

Figure E-6. Trajectories Relative to Massless Comet

with propulsion periods required only on one side of the tail as shown conceptually in Figure E-5.

An estimate of the velocity requirements for each arc of the excursion pattern is obtained from Figure E-7 which shows the two velocity components ΔV_{radial} and $\Delta V_{lateral}$ as functions of the desired

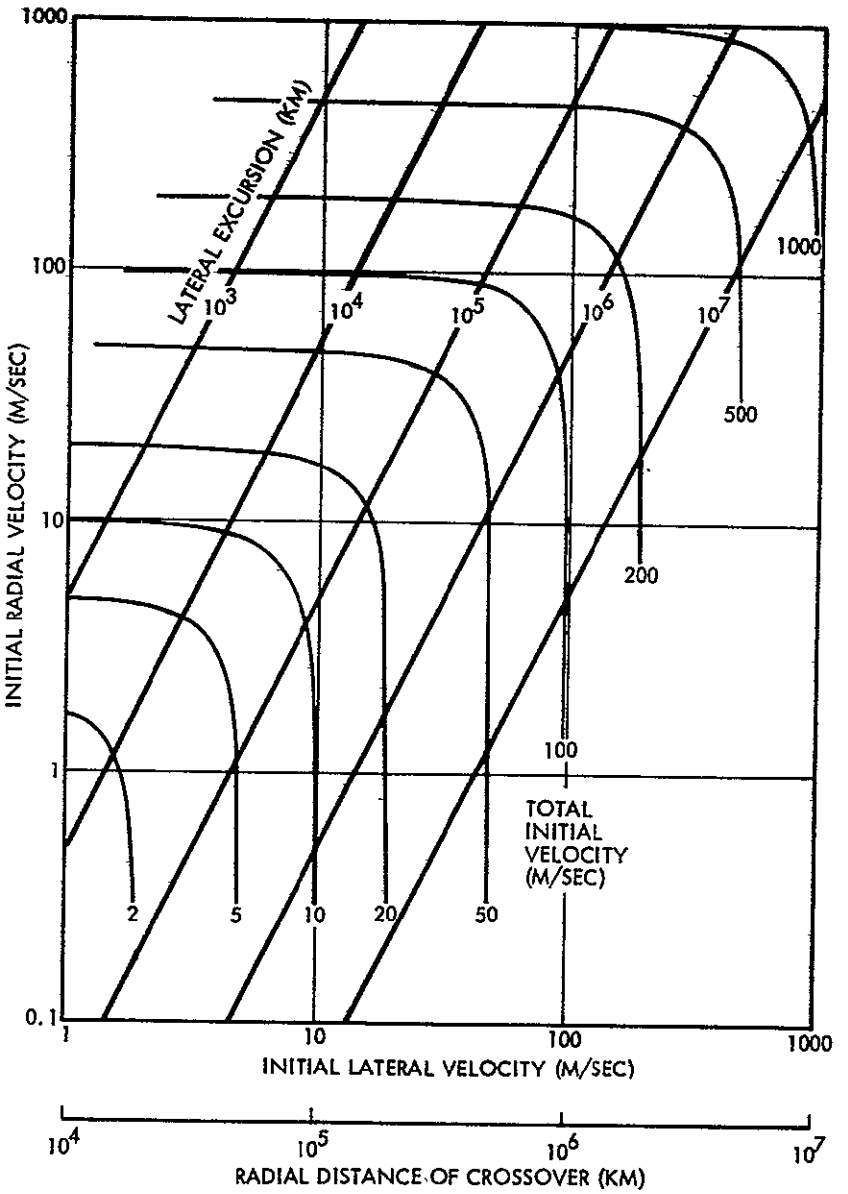

Figure E-7. Maneuver Velocities for Exploration in Vicinity of Comet

maximum lateral excursion and the distance between crossings of the center line, based on the simplifying assumption of a circular 1 AU reference orbit. The radial distance depends on the lateral velocity component only, while the lateral distance is proportional to the radial velocity, given a fixed-lateral velocity. This curvilinear excursion trajectory is particularly useful in daughter (precursor) probe trajectories that can be designed to traverse the double tail in two or even three crossings. (See Figure E-5.) The ΔV chart shows that individual arcs of the tail exploration pattern by the (mother) spacecraft require a pair of velocity increments of 17 m/sec each for a 50×10^3 km lateral and 100×10^3 km radial excursion. The daughter probe requires a velocity increment of 300 m/sec to make a 50×10^3 km lateral excursion and to reach a crossover at 5×10^5 km (based on conditions for a circular, 1 AU reference orbit). The electric stage can readily expend the maneuver energy for ten mapping arcs each requiring about one day of continuous propulsion at the turnaround point.

From these examples of possible approaches to comet exploration by extended maneuvers in the vicinity of the nucleus, coma and tail we conclude that a significant role can be assigned to the electric stage propulsion system after arrival at destination. This consideration is prominent in our selection of an electric stage concept which takes advantage of the available power and propulsion capability at destination, with at least a portion of the payload instruments remaining attached to the stage. The advantage of deploying a subsidiary vehicle (daughter probe) in this mission is also apparent.

APPENDIX F

USE OF THE ELECTRIC STAGE IN AN EROS SAMPLE RETURN MISSION*

F.1 OBJECTIVES

Unmanned missions to the asteroids have been proposed and investigated as part of the overall plan of exploration of the solar system. A principal incentive for landing on an asteroid and retrieving a surface sample for return to earth is the expectation that detailed laboratory analysis of the sample material's chemical composition, crystal structure, surface texture, magnetic characteristics, radioactive state and age can provide essential clues, not available by other means, as to the origin of asteroids and possibly the history and formative processes of the solar system. The results may indicate, for example, to what extent accretion or fragmentation processes have been involved in the formation of asteroids.

Next to the moon the asteroid Eros is earth's closest neighbor in space, and is reasonably accessible to a landing and sample return mission at much smaller propulsive energy than other planetary bodies, owing to the proximity of its orbit and its almost negligible gravity. Such a mission would also be very desirable as a precursor to an unmanned Mars sample return mission being much simpler and less costly.

Solar-electric propulsion is used as the means of primary propulsion during the outbound and return phases. In addition to achieving a highly weight-effective and cost-effective mission it also alleviates launch data constraints, provides flexibility in mission profile selection and guidance, and facilitates execution of the final approach and descent phases under remote control from earth. It also permits extended hover phases in close proximity of the asteroid during which TV images can be transmitted to earth and necessary corrective commands returned to the landing vehicle, with round trip communication delays of 35 to 40 minutes.

*Reference F-1

A fully autonomous vehicle that would perform the final approach and landing at Eros without assistance by ground control would be more complex, more costly and less reliable.

F. 2 MISSION PROFILE

Trajectories, performance characteristics and payload capabilities for one-way and round trip missions to Eros have been investigated by Friedlander, Mascy, Niehoff and others (References F-2 through F-4) for both ballistic and low-thrust propelled vehicles. Figure F-1 shows representative outbound and inbound trajectories of a 1050-day round trip mission with a 50-day stopover at Eros, for the 1977 launch opportunity, based on data obtained by Mascy (Reference F-4). The mission uses solar-electric propulsion both ways, with thrust characteristics and thrust pointing angles optimized to return a maximum amount of asteroid sample material to earth. The vehicle is launched by a Titan 3D/Burner 2 booster and uses 10 kw of initial propulsive power at earth departure. Low thrust is applied continuously during the outbound phase such that the vehicle arrives at Eros with zero relative velocity and can land on the asteroid with almost no additional propulsive effort. Similarly, low thrust is applied continuously during the return trip so as to reduce the approach velocity on returning to earth and the required earth capture maneuver. We assume that the sample return capsule carried by the interplanetary bus vehicle will be inserted into an eccentric earth parking orbit for subsequent retrieval by orbital shuttle, or by a deorbit maneuver, atmospheric entry and parachute landing. This mission profile is shown schematically in Figure F-2 and used as a basis for defining the vehicle design features and operational characteristics to be discussed below. Factors in landing site selection are summarized in Figure F-3.

We note in Figure F-1 that the outbound trajectory departing from earth on 25 February 1977 swings in a wide arc to an aphelion distance of 1.67 AU to achieve the desired velocity matching with the target at the encounter date of 10 July 1978 near perihelion. A gradual plane change necessary to attain the 10.8 degree orbital inclination of Eros is included in the outbound propulsion phase. The return trip departing Eros on 29 August 1978 and arriving at Earth on 12 January 1980 has similar characteristics.

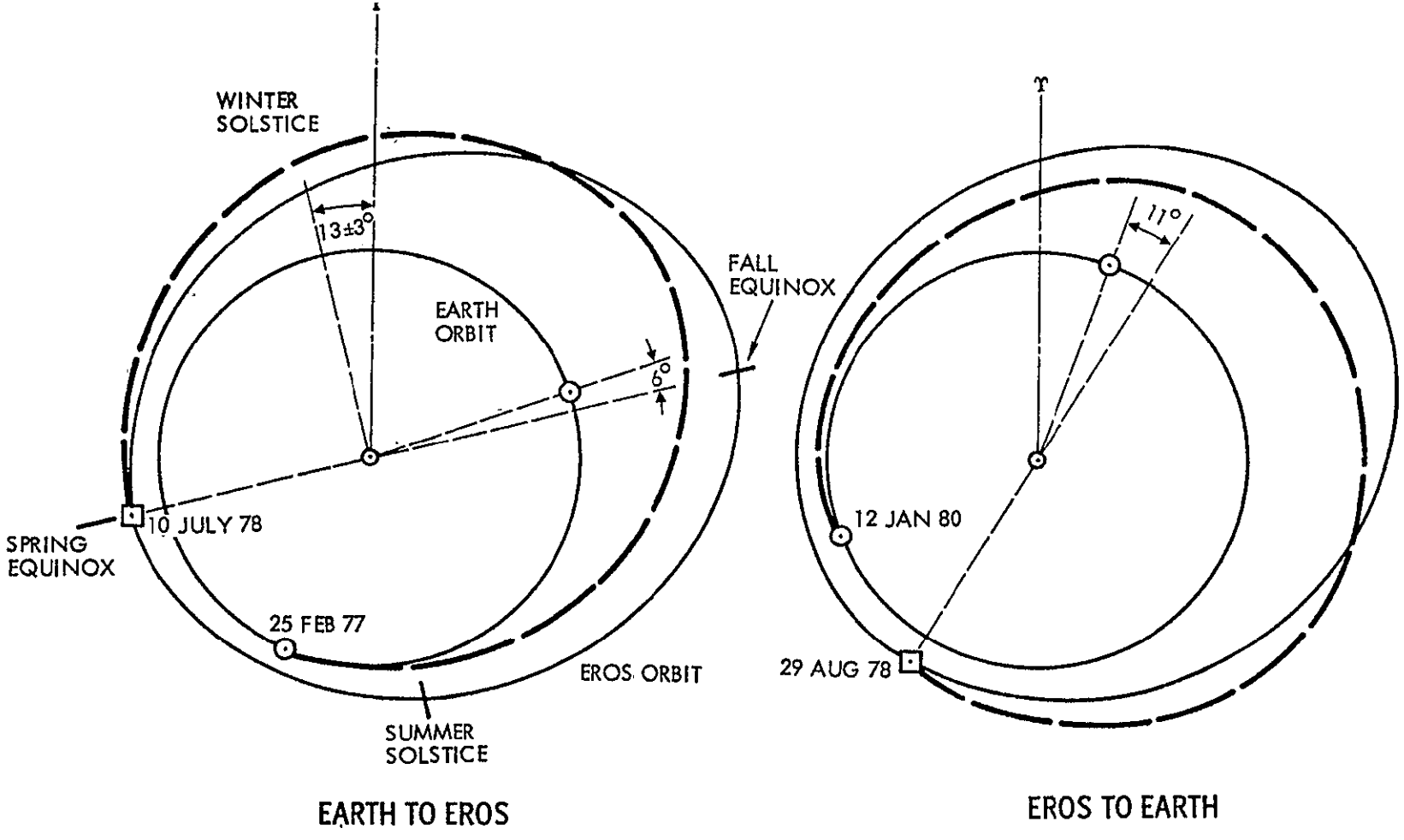

Figure F-1. Eros Round Trip Trajectory from Mascy (Reference F-4)

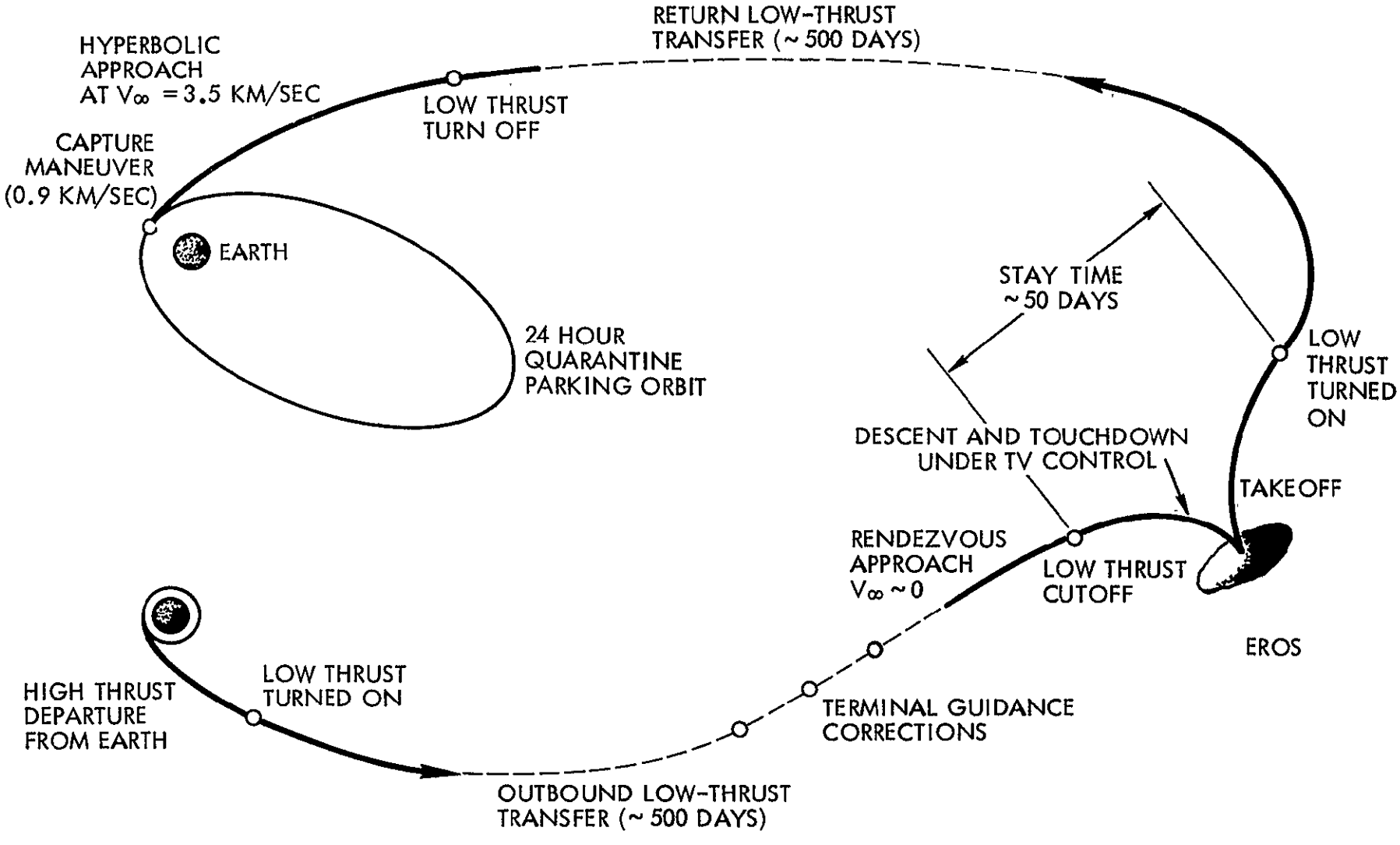

Figure F-2. Eros Round Trip Mission Profile (Schematic)

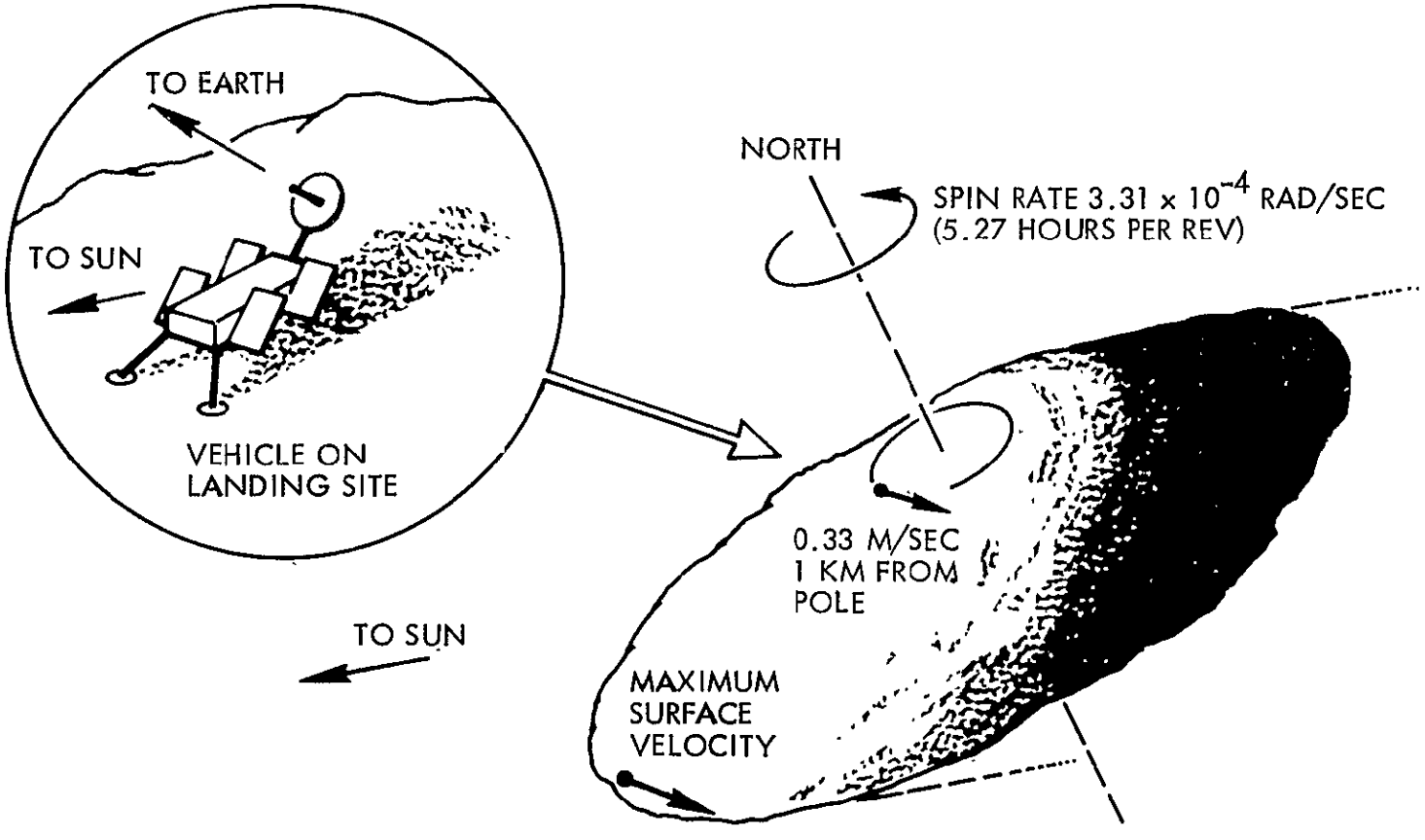

ASSUMED DIMENSIONS 35 x 16 x 7 KM

SURFACE MOTION (ESTIMATES)

MAXIMUM HORIZONTAL VELOCITY	5.8 M/SEC
MAXIMUM RADIAL VELOCITY	1.6 M/SEC
MAXIMUM RADIAL EXCURSION	9.5 KM

EFFECTIVE GRAVITY IN CM/SEC^2 AT TIP OF CIGAR-SHAPED BODY (STALEY, REF 10)

GRAVITY ACCEL	0.264
CENTRIPETAL ACCEL	0.192
DOWNWARD ACCEL	0 072

Figure F-3. Landing Site Selection on Rotating Small Asteroid

Mission opportunities with comparable characteristics occur about every two years. 1977, 1979, and 1981 are favorable mission years. Figure F-4 shows projected sample return capabilities for four mission opportunities from Reference F-4.

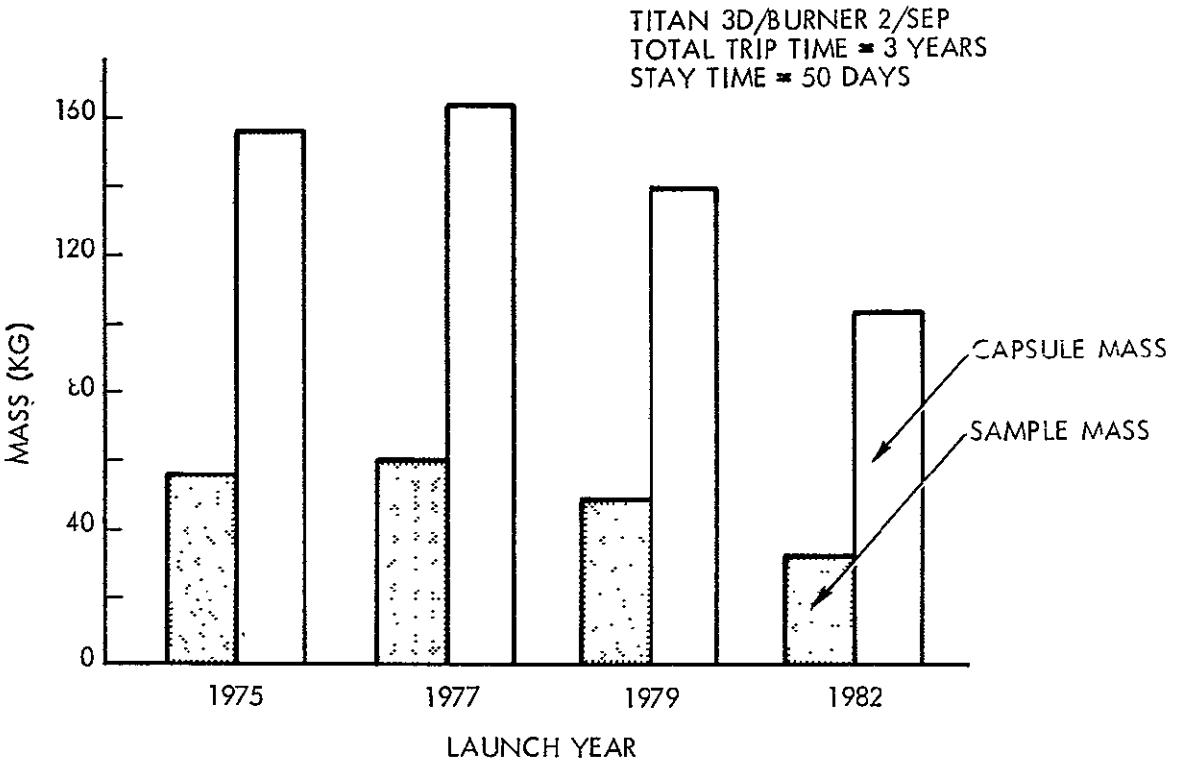

Figure F-4. Launch Opportunity Effect on Returned Mass

A characteristic feature of this class of mission profiles is the large communication range to earth (2.1 AU) and the fact that Earth and Eros are in almost exact opposition at encounter. These conditions do not change much during the 50 day stopover since Earth and Eros move nearly at the same rate. In the reference trajectory the arrival at Eros occurs a short time after syzygy. Communication blackout must be avoided during this critical part of the mission. The earth-sun separation angle subtended at Eros is initially 3 degrees. This gives a margin of only 1 degree from the blackout zone, 2 degrees on both sides of the solar disk, which is assumed under conditions of average solar activity. Actually,

20

since during the late 70's solar activity will be increasing toward a maximum level a larger margin than 1 degree would be desirable. The separation angle increases to 5.5 degrees during the 50 day stopover. Therefore, a 20-day delay in arrival will increase the margin by 1 degree. This can be achieved with only a minor change in payload performance owing to the flexibility of low-thrust missions. A delay in arrival date is also desirable to improve seasonal conditions at the preferred polar site

F.3 VEHICLE CONFIGURATION AND DESIGN CHARACTERISTICS

Conceptual configurations of the solar-electric spacecraft during cruise and after landing are shown in Figure F-5. The vehicle consists of a center structure which houses the electric propulsion module, engineering subsystems, scientific instruments and sample collection tools, and the sample return capsule. Attached to the center body are two pairs of lightweight solar array paddles which are deployed from storage drums in window-shade fashion by means of extendable tubular booms. The flexible landing gear consists of four legs having foot pads lined with crushable material for absorbing impact energy as in the Surveyor spacecraft. Spring released anchoring devices, not shown in the sketch, are used to secure the vehicle's position after touchdown under the extremely small surface gravity of Eros.

A set of four differentially throttleable hydrazine thrusters each with a maximum thrust level of 1 pound are centrally mounted on the underside of the center body. They provide thrust required during the descent and ascent phase and support the vehicle during the extended final hover phase prior to touchdown. With an assumed small surface gravity of 0.5 cm/sec^2 the total hydrazine propellant consumption for a 40-minute hover period is 19 kg for a vehicle of 1700 kg gross weight. The total maneuver sequence performed by the hydrazine thrusters requires about 40 kg of propellant, equivalent to 50 m/sec of ΔV expenditure.

The rollout solar array with each paddle measuring 2 by 14 meters when fully extended provides 12 kw of initial power at 1 AU, 10 kw of which is used to operate the electric propulsion system. The remaining power is used for housekeeping and telemetry and includes a 10-percent margin

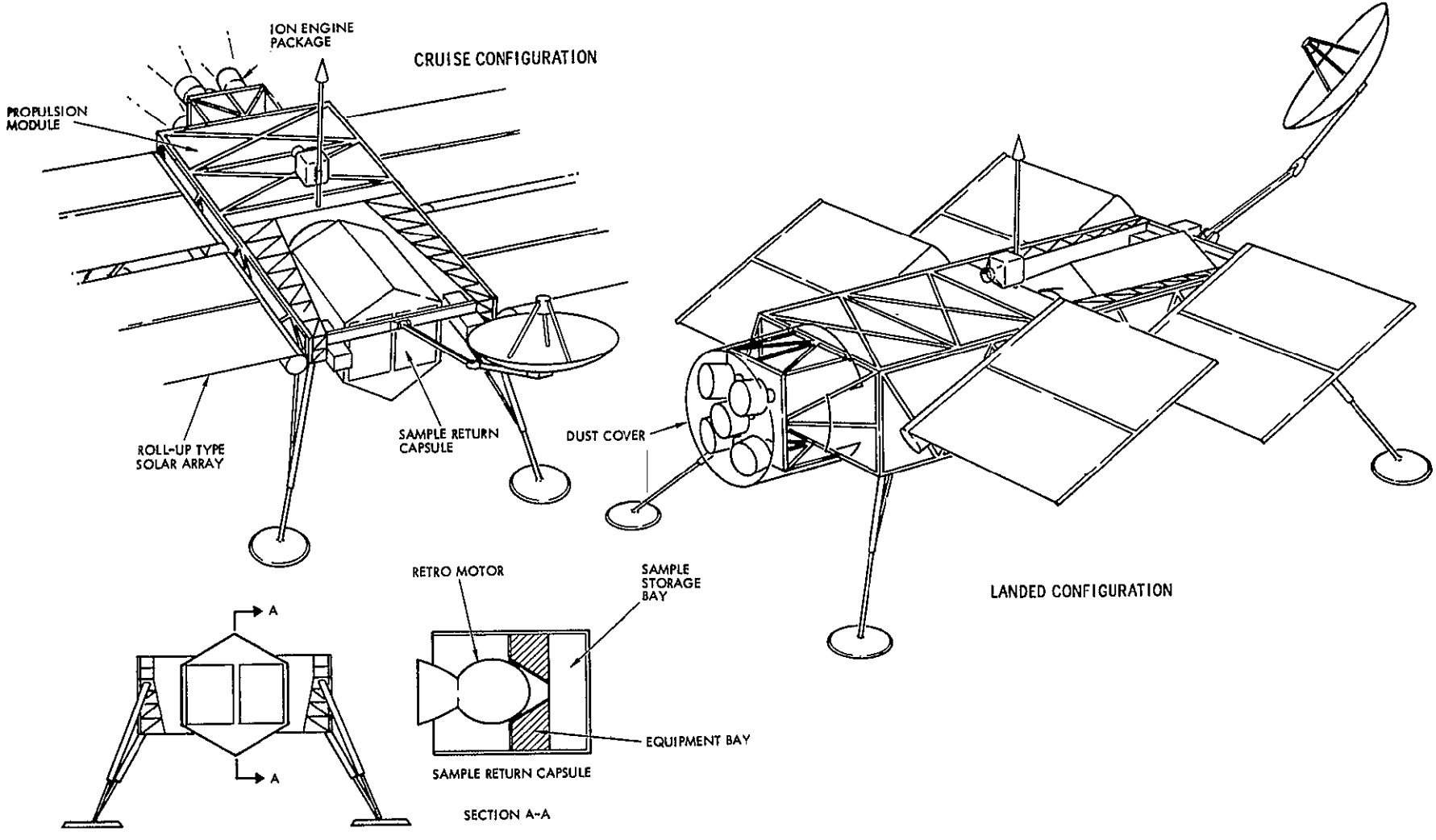

Figure F-5. Solar-Electric Bus Vehicle in Cruise and Landed Configuration

against contingencies such as solar array performance degradation due to solar flares. Prior to landing the paddles are retracted for protection against the landing impact and flying dust. Subsequently small paddle segments are extended to generate power of about 400 watts for surface operations, housekeeping and high-data-rate telemetry of TV pictures. After takeoff from Eros the array is again fully extended for the return cruise.

As shown in the design illustration, the four solar paddles can be rotated around their deployment booms to improve array illumination primarily during the approach, descent and hover phases, and after landing. During the transfer phase small changes in solar array orientation relative to the center body are useful but not required, permitting an additional degree of freedom for optimum thrust vector pointing. During the landed phase array reorientation may be required to accommodate changes in sun elevation. By splitting the array into four narrow paddles instead of two, field-of-view obscuration of optical sensors and the high gain antenna due to paddle reorientation can be avoided.

REFERENCES

APPENDIX F

F-1. Meissinger, H. F., Greenstadt, E. W., "Design and Science Instrumentation of an Unmanned Vehicle for Sample Return from the Asteroid Eros," paper, Asteroid Colloquium held at Tucson, 8-10 March 1971.

F-2. Friedlander, A. L., Vickers, R. S., "A Survey of Missions to the Asteroids," IIT Research Institute Report No. M-3.

F-3. "Digest Report - Missions to the Asteroids," IIT Research Institute, September 1964.

F-4. Mascy, A. C., Niehoff, J., "Sample Return Mission to Eros," paper, Asteroid Colloquium held at Tucson, 8-10 March 1971.

APPENDIX G

ATTITUDE CONTROL SUBSYSTEM CHARACTERISTICS

Characteristics and functional descriptions of the most important subsystem elements of the attitude control system are presented below in list form. Block diagrams and schematic illustrations are attached where applicable.

G. 1 FINE SUN SENSOR ASSEMBLY (FIGURE G-1)

Function	Provides analog signals indicative of sun intensity and sun orientation relative to two orthogonal axes
Description	Each assembly consists of four square solar cells, shaded by a mask plate with a square window, and the associated electronics. Solar cell output voltages are functions of the areas illuminated. Two-axis angular information is derived from differential voltage measurements. Sun intensity reference is provided by the sum of all four output signals.
Selected characteristics	$\pm$10 degree field of view about each axis $\pm$0. 1 degree (3σ) null accuracy (each axis) $\pm$10 percent linearity (each axis)
Mass (kg)	0. 30 kg (including electronics)
Power requirements	Input: 0. 4 watt Output:
Location on spacecraft, field of view, articulation requirements	The baseline system includes two sensor assemblies. One assembly will be mounted on the rotating solar-array support structure. A second one is installed on the stage body on the side facing the sun. Increased field of view requirements can be met without design changes by installing additional modules.
State-of-the-art source program (technology or spacecraft)	The assembly is a new design. However, the primary sensor elements have been used in most spacecraft applications requiring sun reference with accuracies in the 0. 5 to 0. 1 degree range.

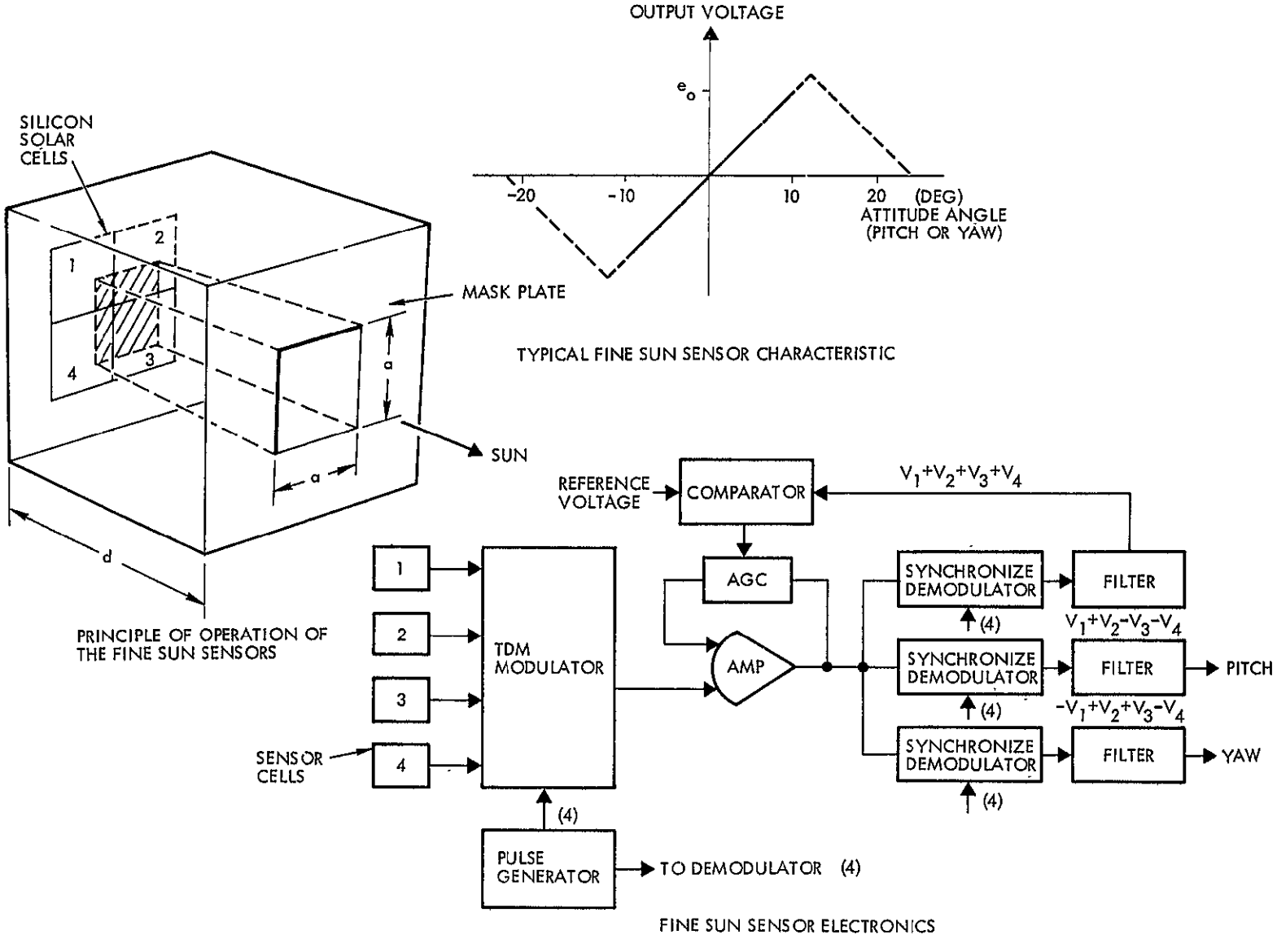

Figure G-1. Fine Sun Sensor Block Diagram

Modifications required for multi-mission compatibility	The modular concept adopted provides highest degree of flexibility for meeting redundancy and field of view requirements for all missions. Sensor signal selection and switching is managed by the stage's digital computer in response to real time or stored program instructions.
Technology improvements required and associated costs	Performance requirements can be met with present state-of-the-art components.
Number required per stage	Two (baseline system)
Alternate approaches	Two-axis digital aspect sensors
Reason for selection	Analog devices are simpler and provide required resolution and accuracy with high reliability. AGC can be easily implemented. Sensor performance and quantization are less dependent on solar constant changes.

G. 2 COARSE SUN SENSOR ASSEMBLY

Function	Provides two-axis indications of sun direction for acquisition purposes over a π-steradian field of view.
Description	The coarse sun sensor consists of two pairs of solar cells mounted back to back with plano-convex lenses in optical contact with the cell surfaces. Shading is used to restrict the field of view to π-steradians. Solar cells are connected with opposing polarities across a low-resistance load producing an approximately linear output within $\pm$20 degrees of null (each axis).
Selected characteristics	$\pm$10 percent linearity over $\pm$20 degrees about null plane (each axis) Null accuracy better than $\pm$one degree π-steradian field of view
Mass (kg)	0. 15 kg
Power requirements	Input: None Output: None

Location on spacecraft, field of view, articulation requirements	The baseline comprises four coarse sun sensor assemblies. Two units are located on the solar and two on the anti-solar side of the stage. π-steradian unobstructed viewing angles are required.
State-of-the-art source program (technology or spacecraft)	Flight-proven hardware available (OGO)
Modifications required for multi-mission compatibility	None
Technology improvements required and associated costs	Performance requirements can be met with present state-of-the-art components.
Number required per stage	Four
Alternate approaches	None
Reason for selection	Flight experience, simplicity, low cost.

G. 3 STAR SENSOR ASSEMBLY

The star sensor is an instrument of the Mariner Mars type gimballed mechanically to produce clock-angle rotations of the instantaneous field of view. Cone-angle displacements are obtained by electronic offset in the nonsensitive direction (see Figure G-2).

This allows tracking several stars during each mission. The cone-angle offset of the field of view and the clock-angle range are chosen to ensure that at least one bright star is available at all times for each particular mission.

Function	Provides single-axis analog attitude information relative to stars within the brightness range from 0. 04 to three times the Canopus brightness.
Description	The assembly consists of an image dissector tube, deflection yoke, wide field-of-view lens, baffle, diaphragm, filters, sun sensor activated shutter and redundant electronics for beam deflection and signal processing. (See Figure G-3.)

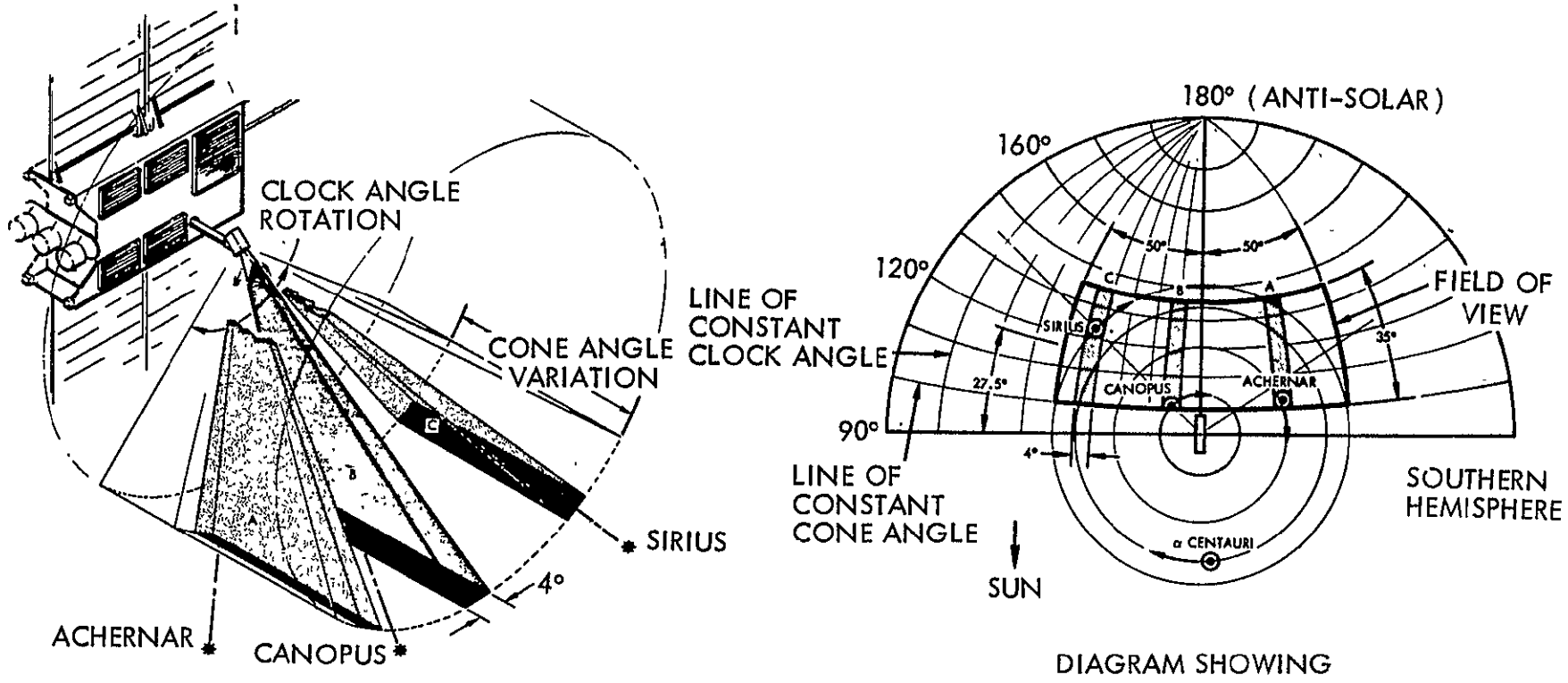

Figure G-2. Star Sensor Concept

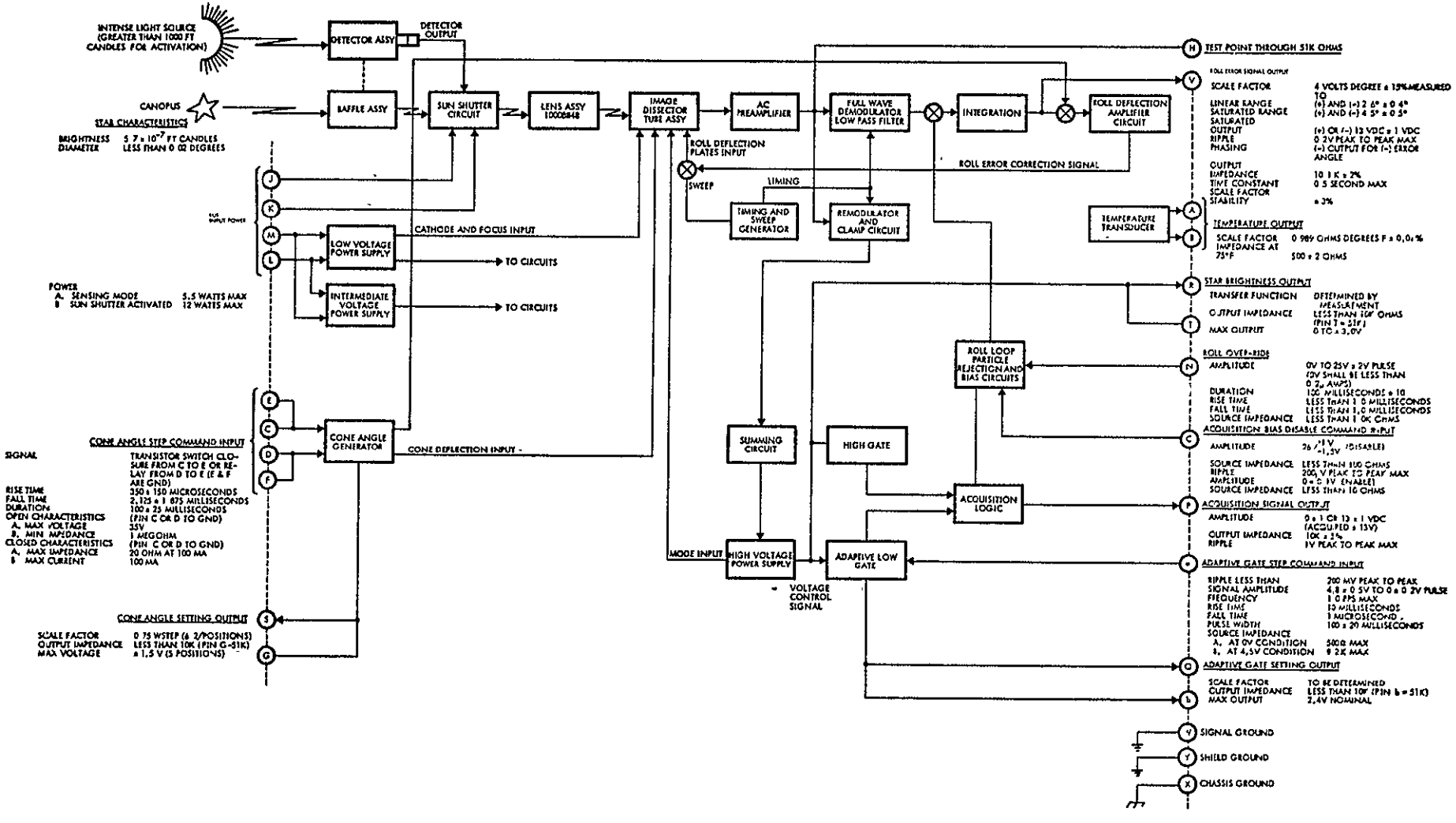

Figure G-3. Star Sensor Block Diagram

Selected characteristics	Shown in Table G-1
Mass (kg)	4.55 kg
Power requirements	Input: 5.5 watt (tracker only) 6.5 watt (sun shutter, peak) Output:
Location on spacecraft, field of view, articulation requirements	The baseline system includes one star tracker mounted on a gimbal drive assembly (in anti-solar side of stage). Mechanical gimbal axis of the drive is mounted parallel to roll axis of the stage. The electrical gimbal axis of the tracker is normal to the mechanical gimbal axis.
State-of-the-art source program (technology or spacecraft)	The proposed star sensor was developed for and flown on the Mariner Mars 1969 spacecraft.
No modifications are required for multi-mission compatibility	Gimballing capabilities provide a high-degree of flexibility, since multiple stars can be tracked on each particular mission. Low-drift gyros are used as primary roll references. Star tracker data are used for updating and compensating the gyros.
Technology improvements required and associated costs	Improvements in electronic technology and experience obtained with other star trackers are expected to cause significant improvements of reliability and reductions of weight and power.
Number required per stage	One (with redundant electronics)
Alternate approaches	None
Reason for selection	This instrument type was selected because of its low weight and power requirements. Other types of star sensors can provide greater accuracies, but the penalties involved are not justified on the basis of pointing accuracy requirements of the SEMM stage.

Table G-1. Performance Summary of the Mariner Type Canopus Star Tracker

Tracking accuracy	
Short term	0.002 degree (single axis sensor only)
Long term	0.05 degree (single axis sensor only)
Tracking star brightness range	0.04 to 3.0 x Canopus brightness
Field of view	
Instantaneous	1.05 x 11 degrees
Scanned	4 x 11 degrees
Acquisition (electrically gimballed)	9 x 35.8 degrees
Electronic gimbal ranges	
Sensitive axis (roll)	±3 degrees from null axis
Nonsensitive axis	±17.9 degrees from tracker axis

G.4 GYRO ASSEMBLY (FIGURES G-4 AND G-5)

Function	Each gyro assembly module provides redundant single-axis inertial rate and attitude information in digital form. Also, the assembly can provide a two-axis reference by operating the two gyros simultaneously.
Description	Each module consists of two Northrop GI-K7G gas-bearing single-degree-of-freedom gyros (in a redundant configuration) and their associated power conversion and signal processing electronics. The gyro unit utilizes a ceramic hydrodynamic gas-bearing operating in a beryllium float constrained along the output axis by means of a taut wire suspension system. The unit includes a moving coil pickoff and a permanent magnet torquer. The signal processing electronics uses a combination of analog gyro torquing and voltage-to-frequency conversion to provide a digital output. Heaters are provided for close temperature regulation.
Location on spacecraft, field-of-view, articulation requirements	All modules mounted in temperature-controlled equipment compartment with input axes aligned with stage's control axes.

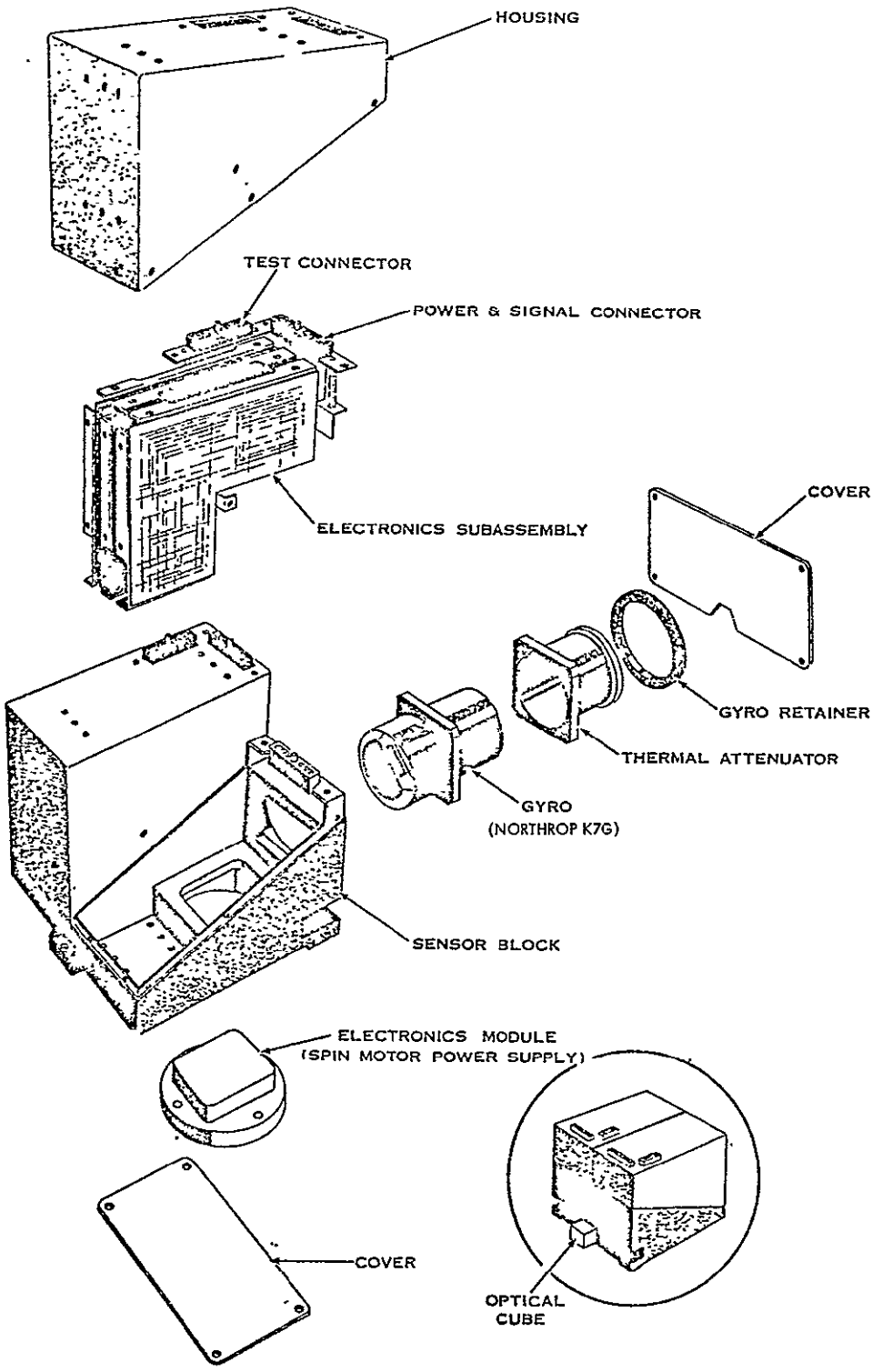

Figure G-4. Gyro Assembly Module

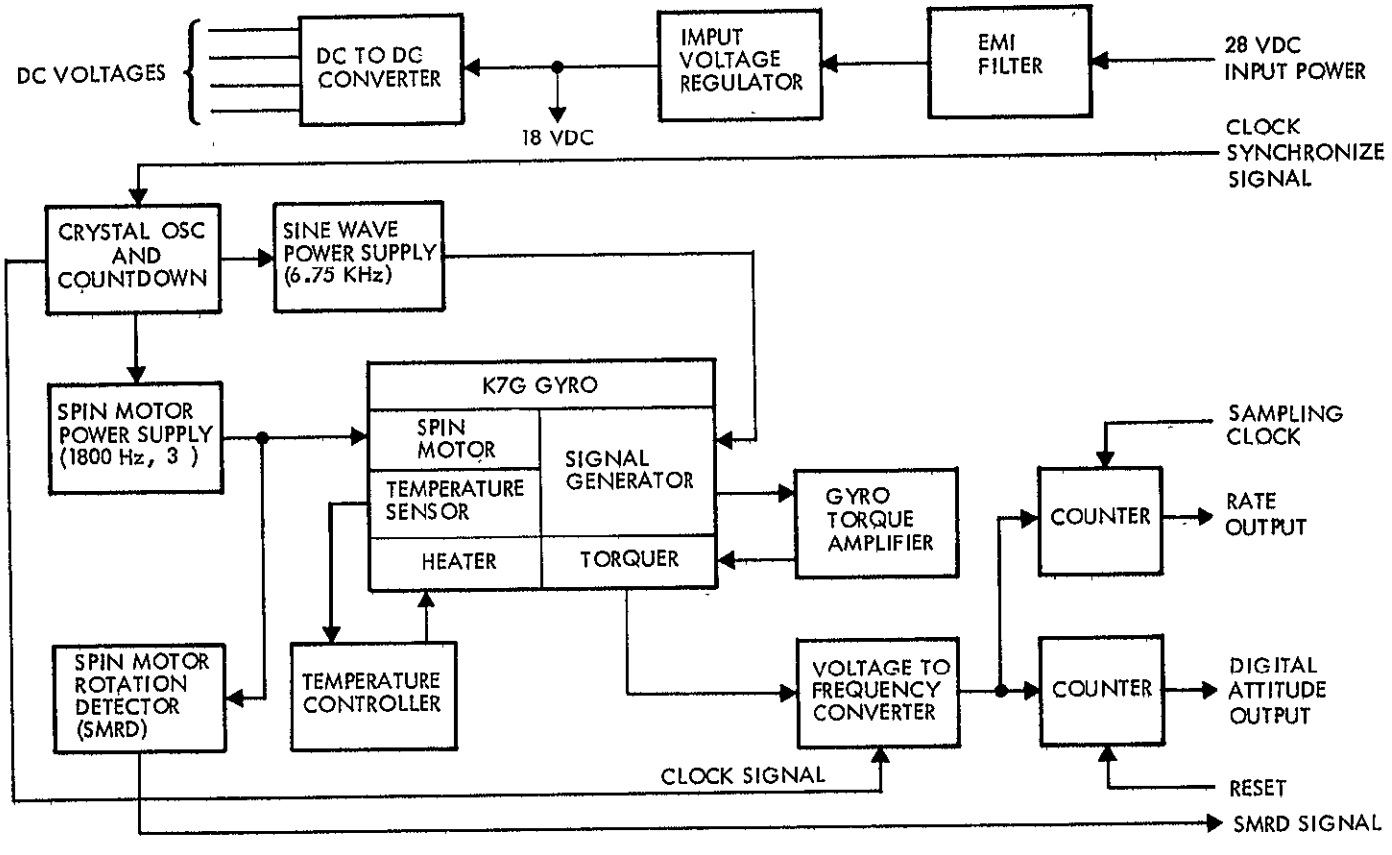

Figure G-5. Gyro Electronics Block Diagram

State-of-the-art source program (technology or spacecraft)	The GI-K7G gyro is a scaled-down and simplified version of the GI-T1B gyro used in the Minuteman ICBM system. The GI-K7G gyros are in production for the C5-A USAF transport and an ESRO satellite program.
Modifications required for multi-mission compatibility	None required. The proposed modular concept provides a very high-degree of flexibility and minimizes interface problems.
Technology improvements required and associated costs	None required. Performance improvements are expected as a result of experience in the C5-A and ESRO programs.
Number required per stage	One module - probes, rendezvous and flyby missions - (input axis along roll axis of stage). Three orbiter and lander missions.
Alternate approaches	Conventional ball-bearing gyros. Non-redundant configurations (i.e., single rate gyro package as in SEMM-1 or three-axis, non-redundant IRU).
Reason for selection	Gas bearing gyros have been selected because of their higher reliability (MTBF greater than 3.7×10^5 hour based on 3×10^6 hour experience with GI-T1B gyros in the Minuteman program). The GI-K7G gyros have the advantages of low-power consumption and small size and weight. The modular concept selected provides the following options without redesign or requalification. • Redundant, single-axis (roll) reference (one module) • Non-redundant, two-axis reference (one module) • Redundant, three-axis reference (two modules). Four-gyro configuration allows single-gyro failure • Redundant, three-axis reference (three modules). Six-gyro configuration allows failures of any three gyros. Automatic failure detection and correction can be implemented by having more than four gyros in operation • Redundant, orthogonal, three-axis reference (three modules). Only one gyro (on each axis) is allowed to fail without catastrophic results

G. 5 CONTROL PROCESSOR ASSEMBLY (FIGURE G-6)

Function	The control processor assembly provides logic, decision and computing capabilities to the control subsystem on a priority interrupt basis, and also, provides support to other subsystems of the stage on a non-cyclic basis. A summary of control functions is given in Table G-2.
Description	The control processor assembly consists of a redundant set of two internally cross-strapped, general purpose digital computers. Each computer package consists of a processor, input/output, memory, and power supply subassemblies.
Selected characteristics	See Table G-3
Mass (kg)	8.0 kg
Power requirements	Input: 17 watts Output:
Location on spacecraft, field-of-view, articulation requirements	Equipment compartment
State-of-the-art source program (technology or spacecraft)	The Honeywell HDC-300 series computers will be used in the ATS program. Considerable experience with computers of this class is expected to be available within the next five years.
Modifications required for multi-mission compatibility	None. Memory size can be increased (if required) without redesign by simple incorporation of additional 4-K memory subassemblies to the basic modules.
Technology improvements required and associated costs	Significant increase in reliability and decrease in weight and power are expected as results of improvements in electronic technology.
Number required per stage	One redundant, internally cross-strapped, assembly per vehicle.
Alternate approaches	Two Honeywell HDC-400 series computers.
Reason for selection	The HDC-400 series machines are expected to be superseded by computers of the HDC-300 type because of their higher reliability.

Reason for selection (continued)

The HDC-300 series is about 50 percent lighter and requires about the same power.

Selection of a baseline machine requires detailed tradeoffs exceeding the scope of the present study. The HDC-300 has been chosen as an example of the next generation of miniature spaceborne computers.

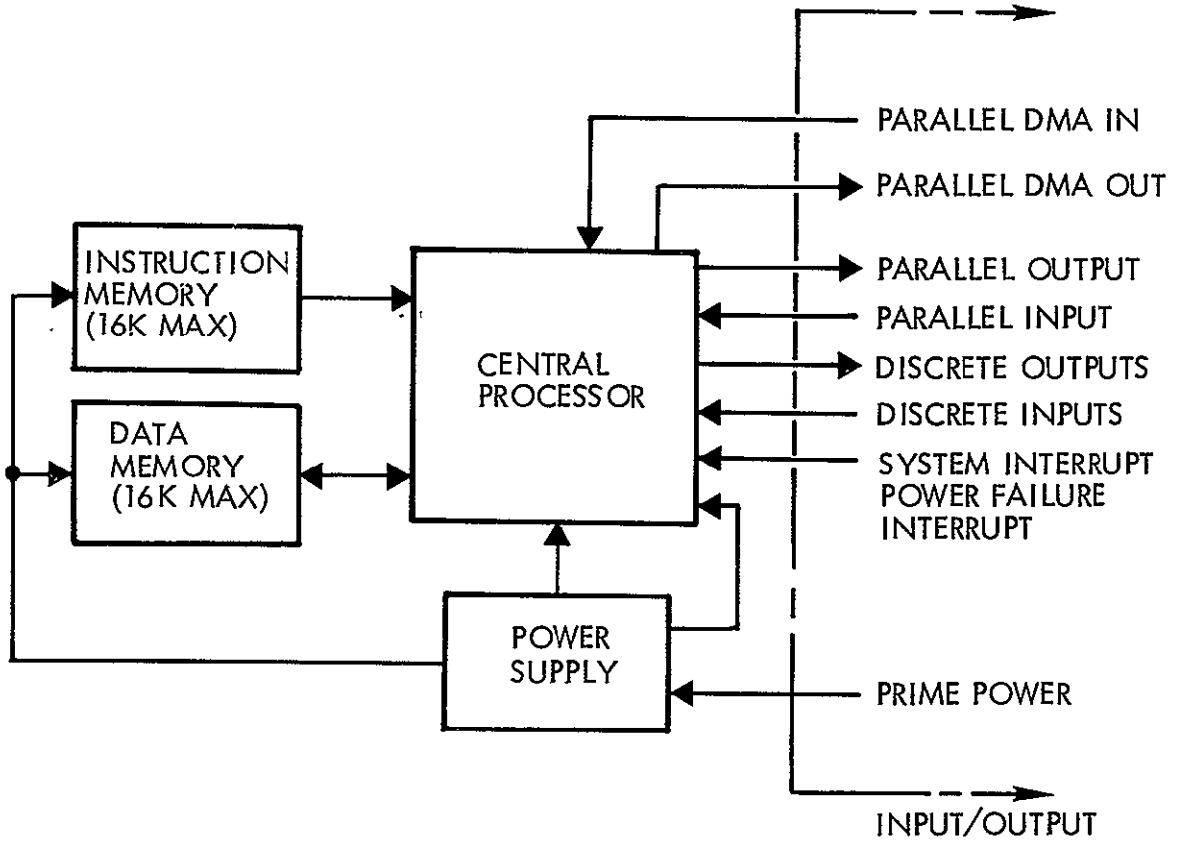

Figure G-6. Control Processor Assembly Block Diagram (Redundancy and Cross-strapping not shown)

Table G-2. Control Subsystem Functions Performed by CPA

Executive	Input/Output
Program control	Input data processing
Mode control	Telemetry input data processing
Computer self test	Output data processing
System test	Telemetry output data processing
Attitude Determination	**Attitude Control**
Sun sensor signal processing	Attitude error computation
Sun sensor biasing and switching	Control laws (PWM) (proportional with compensation)
Star tracker data processing	AC thruster select and control logics
Star tracker electronic gimbal program generation	TVC select logic
Star tracker mechanical gimbal program generation	TVC command generation
Star search and identification	Steering equations
Star acquisition	**Pointing**
Gyro data processing	Antenna gimbal command generation
Gyro drift compensation	Experiment package orientation
Attitude data filtering	Solar array orientation
Alignment updating	
Failure, detection, diagnosis and correction	

Table G-3. Preliminary CPA Characteristics (Each non-redundant Computer)

Processor technology	Low V_T P-channel MOS, LSIC
Memory technology	Miniature plated wire
Word length	16 bits
Add time	5 microseconds
Multiply time	21 microseconds
Divide time	65 microseconds
Processor part count	15 LSIC's, 21 standard IC's
Processor size	One board, 5 x 6 inches
Memory size	4 k
Compatibility	Input/output interface is compatible with the Honeywell commercial computers H-316 and DDP-516 I/OS
Built-in test	Go/no-go confidence test is provided

APPENDIX H

POWER PROCESSOR INPUT FILTER MASS

To establish the weight penalties projected for the input filters, we assumed a preliminary EMC specification for the stage. This specification is based upon scaling of existing specifications for Pioneer F and G spacecraft and TOR-1001-4 to the projected stage system requirements. A more detailed estimate of filter mass can only be made when payload instrument and engineering subsystem requirements and constraints will have been established in more detail.

Figure H-1 and H-2 show the narrowband and audio-conducted interference limits for the preliminary electric stage design, the TOR-1001-4 and the Pioneer F and G specifications. The basic difference in these specifications lies in the 10-1000 kHz range.

To meet these requirements without introducing significant weight or efficiency penalty a two-stage input filter as illustrated in Figure H-3 is used. Figure H-4 presents the attenuation characteristics for such a two-stage input filter designed for controlled resonant peaking. The characteristic shows a 4 db peak at 800 Hz. A conventional single-stage input filter could have peaks as high as 20 db or more unless some resistive damping is placed in the capacitor or inductor causing significant power losses.

Figure H-5 shows the estimated mass of the input filter for the three types of EMC specifications. The SCR unit requires a higher filter mass than the transistorized PPU because the ripple frequency is 20 kHz while the ripple frequency for the parallel transistor device is 200 kHz. The ripple frequency of the SCR device can be increased with further development.

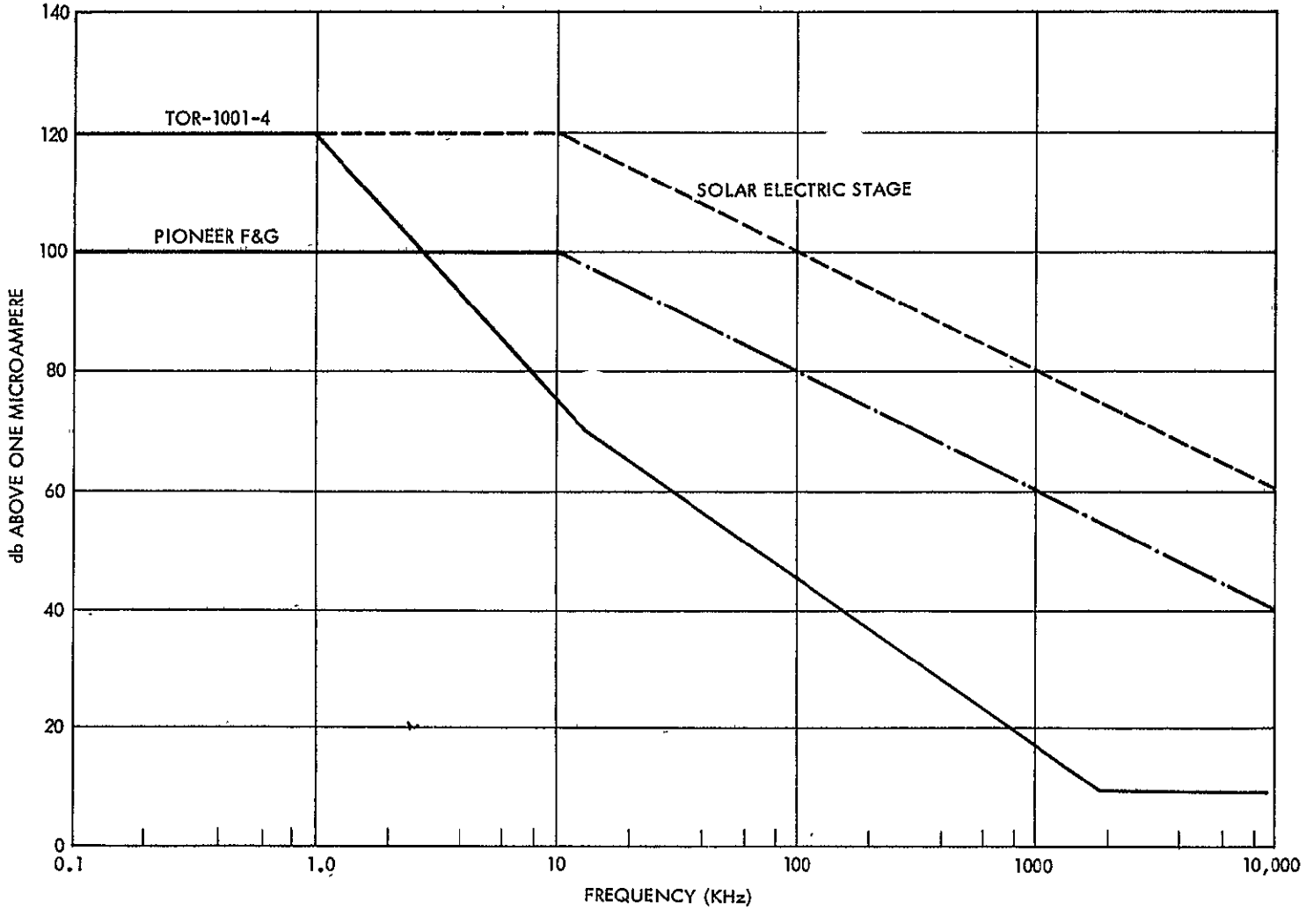

Figure H-1. Narrowband-Conducted Interference Limits

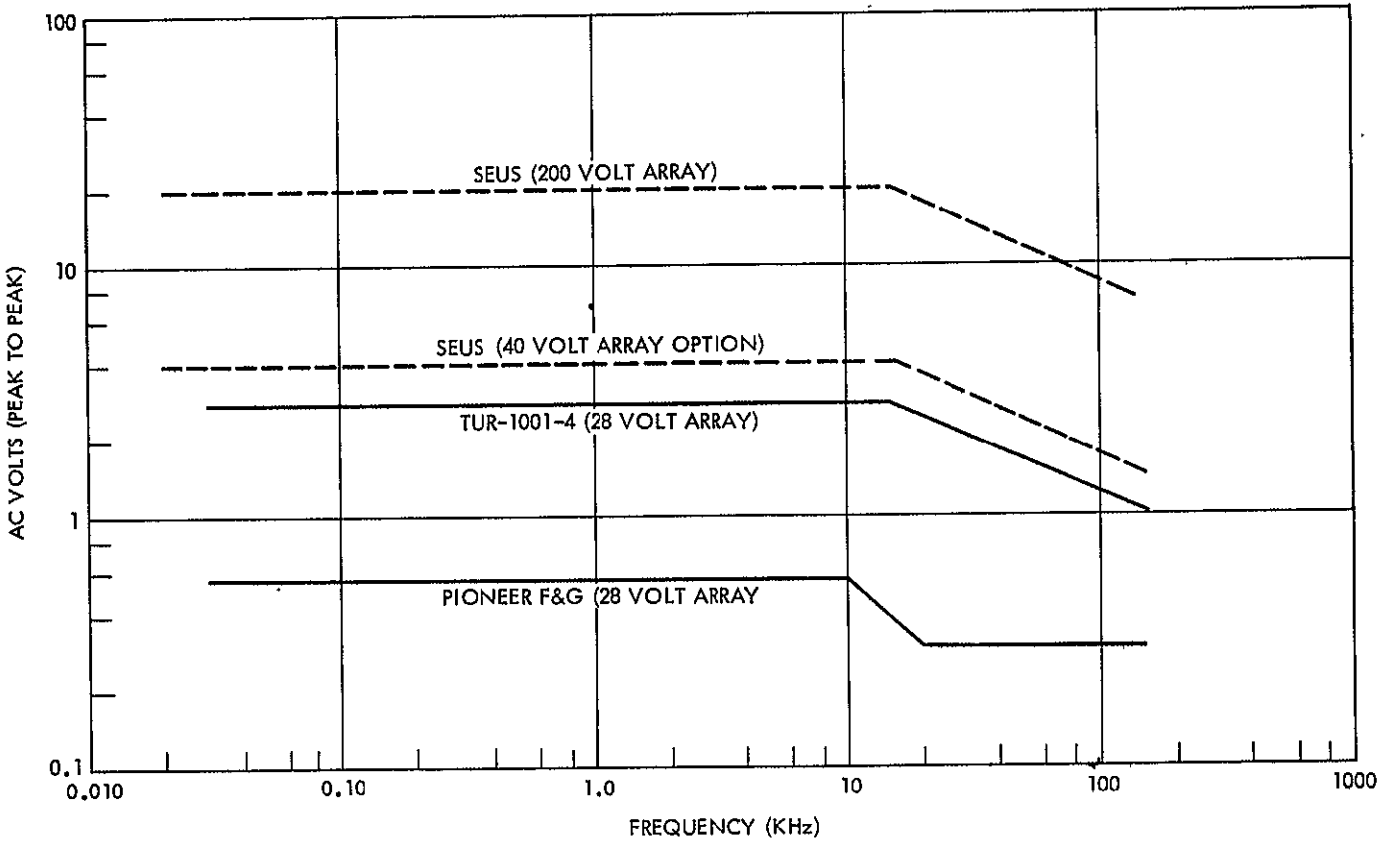

Figure H-2. Audio-Conducted Susceptibility Limits

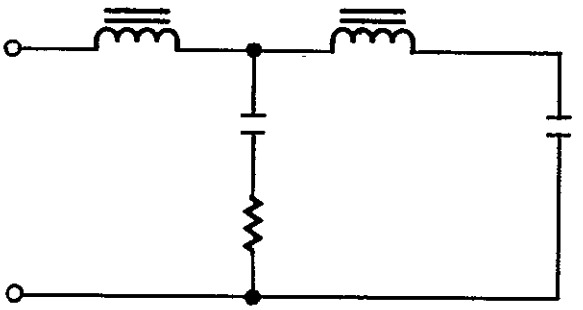

Figure H-3. Two-Stage Input Filter for Power Processor with Controlled Resonant Peaking

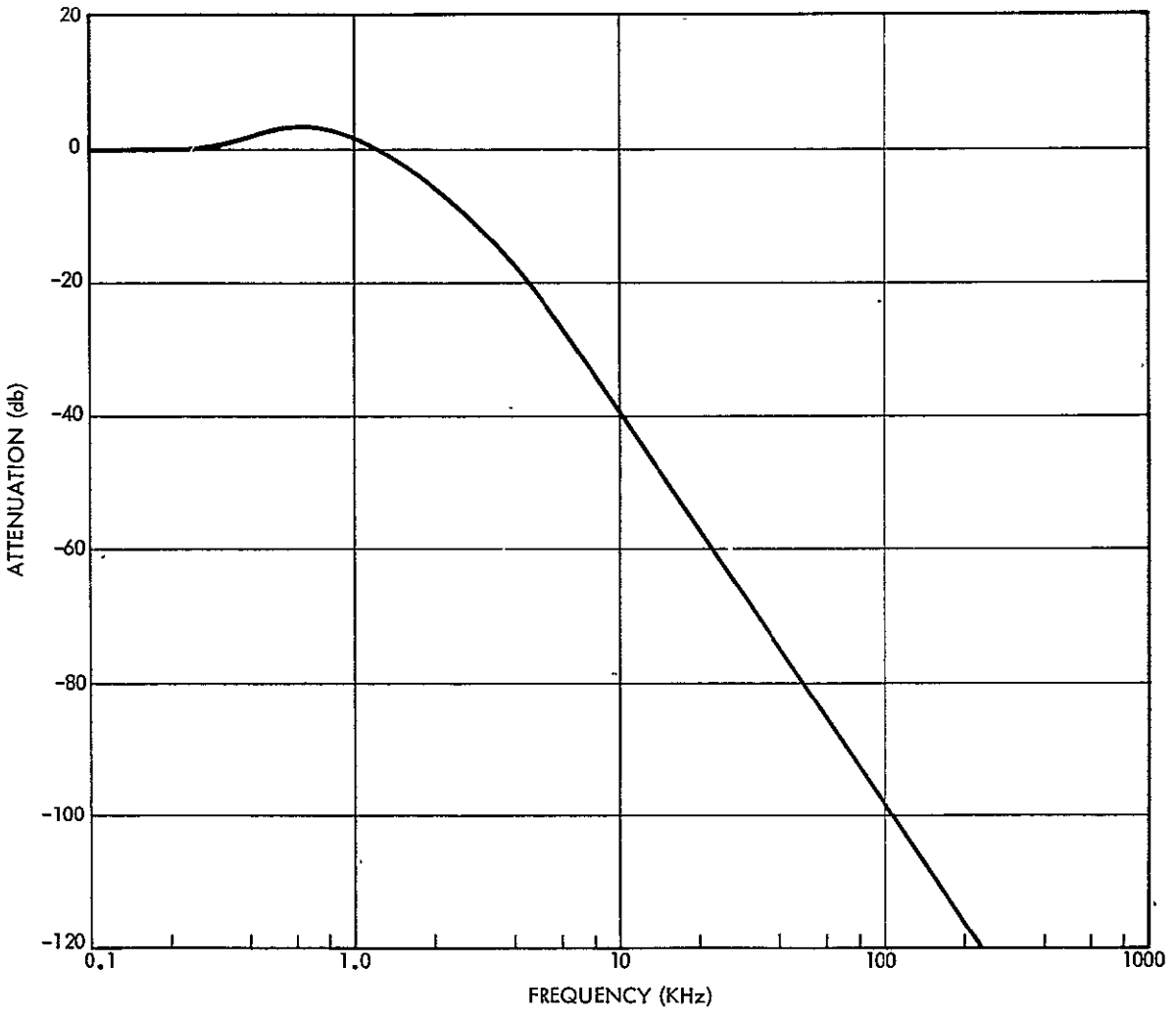

Figure H-4. Attenuation Characteristic of Two-Stage Input Filter

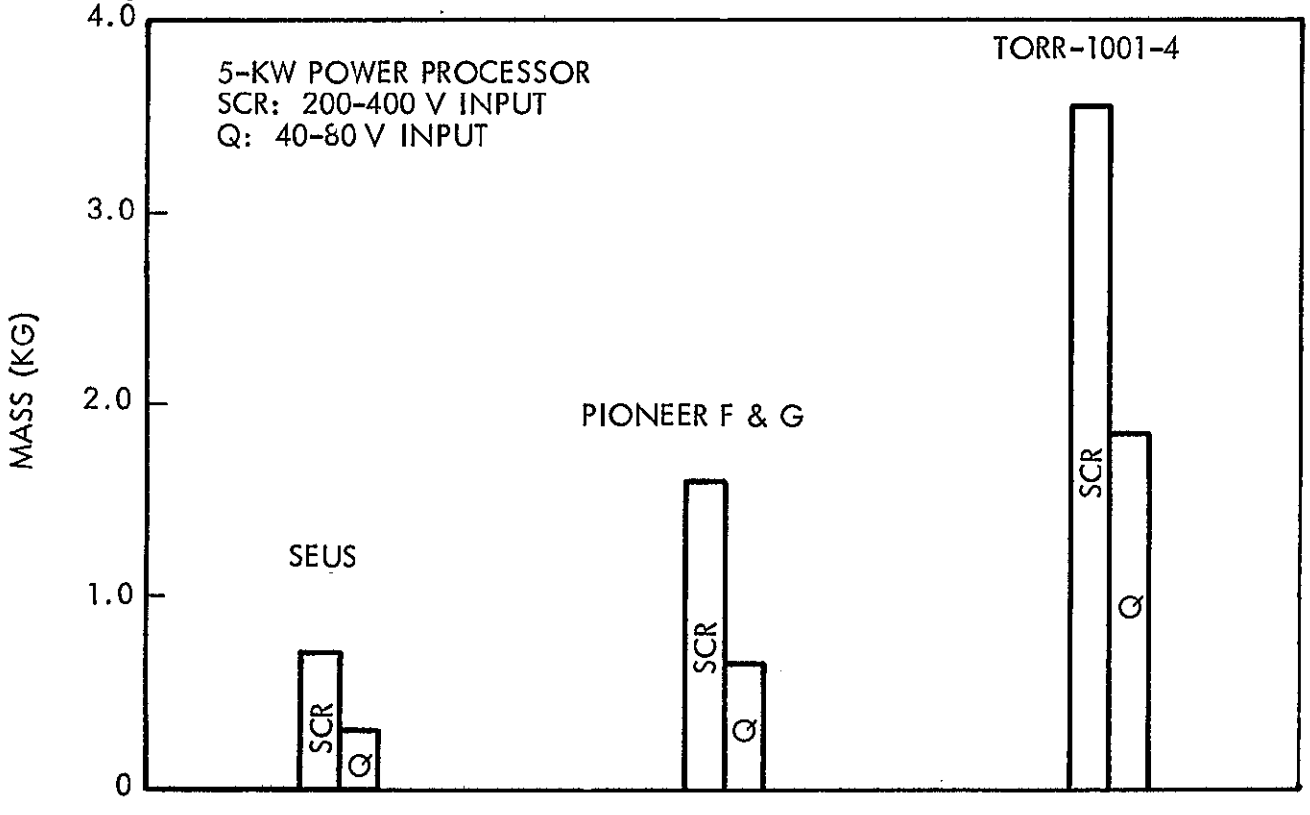

Figure H-5. Comparison of Input Filter Mass for SCR and Transistor (Q) Power Processor for Different EMC Specifications